Journal of Mechanical Design. Received September 05, 2025;
Accepted manuscript posted January 5, 2026. doi:10.1115/1.4070757
Copyright © 2026 by ASME; reuse license CC-BY 4.0

Check for updates

Olivia Vitale[1]
Sibley School of Mechanical and Aerospace Engineering,
Cornell University, Ithaca NY
email: ov35@cornell.edu

Rebecca McCabe
Sibley School of Mechanical and Aerospace Engineering
Cornell University, Ithaca, NY
email: rgm222@cornell.edu

Aisha Brundan
George W. Woodruff School of Mechanical Engineering
Georgia Institute of Technology, Atlanta, GA
email: abrundan3@gatech.edu

Yashaswini Mandalam
School of Electrical and Computer Engineering
Cornell University, Ithaca, NY
email: ym569@cornell.edu

Ana Sofia Alonso Munera
Department of Mechanical and Aerospace Engineering
Princeton Univeristy, Princeton, NJ
email: aa7893@princeton.edu

Maha N. Haji
Department of Mechanical Engineering
University of Michigan, Ann Arbor, MI
email: mhaji@umich.edu

Design, build, and analysis of small-scale wave energy converter prototypes

This work details a methodology for the design of small-scale wave energy converter (WEC) prototypes, consolidating design knowledge and techniques while contributing to the production of higher-quality, fundamental WEC research. The methodology is applied in the design, build, and deployment of two WEC architectures: heaving point absorbers (PAs) and oscillating surge WECs (OSWECs). Relevant design considerations are described in depth, including testing facility, fluid regime, model physics, mechanical design, and electrical design. The design process is validated through experimental results, and recommendations are made for improvements on small-scale WEC systems. Minimizing friction at the small-scale is a known challenge, but the implemented rack and pinion powertrains satisfied requirements. Additionally, electrical current measurement resolution becomes a limiting factor at the small-scale, prohibiting effective controls and electrical power generation. Almost all components were purchased off-the-shelf or machined using standard tools (bandsaw, drill press, hand tools), with a few CNC-milled, waterjet, and lasercut components. A table of generalized, universal requirements for small-scale WEC development is provided. This methodology serves as a guide for small-scale WEC design and testing, improving design techniques and datasets generated from experimentation.

Keywords: small-scale prototyping, wave energy converters, design for model validation

Accepted Manuscript Not Copyedited

Downloaded from http://asmedigitalcollection.asme.org/mechanicaldesign/article-pdf/doi/10.1115/1.4070757/7582635/md-25-1640.pdf by guest on 05 January 2026

1 Introduction

Wave energy is a nascent renewable energy technology with extreme potential. Ocean waves are consistent [1], predictable [1,2], and 100x more power dense than wind [3,4]. In the United States waters alone, there is enough extractable power to meet 34% of the country's electricity consumption [3,5,6]. A few full-scale WEC devices have been successfully deployed [7–10], but WECs as a whole are still not commercially viable [11,12]. To become economically competitive with other renewables, wave energy needs significant technological innovation [13].

1.1 Wave Energy Converters.

WECs extract power from the oscillatory motion of ocean waves. Unlike solar and wind, there is currently no design convergence for WECs, and several proposed WEC architectures are actively in research and development [14–18]. A floating body can be hydrodynamically excited in six degrees of freedom, all of which hold power available for extraction. Two common designs are heaving point absorbers (PAs), which move up and down with wave motion, and oscillating surge WECs (OSWECs), which rotate about a hinge. Along with different mechanical designs, there are several possible power take-off (PTO) methods, including hydraulics, pneumatics, gearboxes, pulleys, and more. Figure 1 shows a simplified version of a PA and OSWEC system.

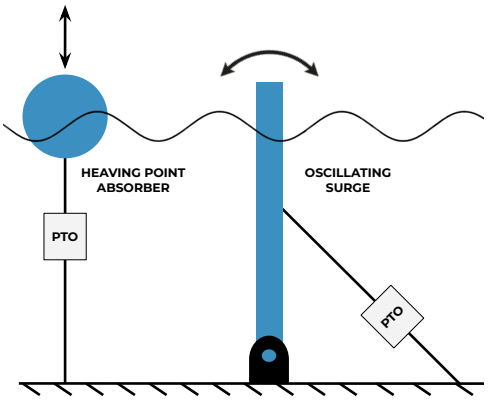

Fig. 1 Simplified example of a heaving PA (left) and OSWEC (right).

1.2 Small-Scale Prototyping.

With the rise of modern technology, numerical and computational modeling have increased in

[1]Corresponding Author.
Version 1.18, December 8, 2025

Journal of Mechanical Design. Received September 05, 2025;
Accepted manuscript posted January 5, 2026. doi:10.1115/1.4070757
Copyright © 2026 by ASME; reuse license CC-BY 4.0

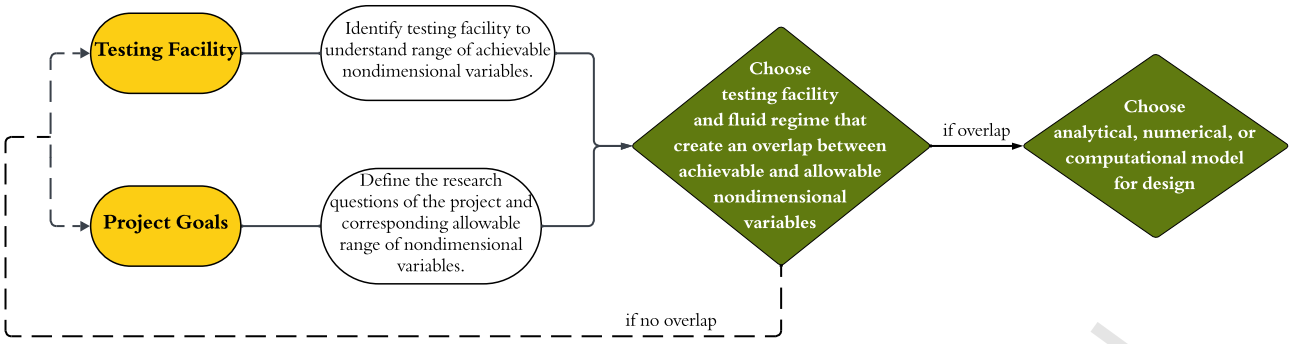

Fig. 2 Flow chart of overarching design considerations.

popularity, allowing researchers to create, test, and iterate complex designs within a digital environment [19–21]. In the context of wave energy, such models are particularly valuable during the early design stages of development, as WECs are costly to manufacture at full-scale. Hydrodynamic numerical simulations have been widely used to optimize WEC hull geometries, PTO systems, and mooring design [22–24]. However, these simulations have notable limitations. Fluid dynamics simulations are computationally expensive, an issue that compounds when integrating them in optimization workflows, multi-body simulations, or when modeling across diverse oceanic conditions. While high-performance computing can mitigate some of these challenges, it introduces further demands in terms of computational infrastructure and expertise.

Although computational models can predict hydrodynamic behavior with high accuracy, they do not give insights into practical challenges that arise with implementing new technology [25–27]. For instance, specifying an exact geometry or center of mass in a model is straightforward, but achieving such precision in a manufactured prototype is more difficult. This discrepancy also applies to parameters like stiffness, mass moment of inertia, and position of a physical device. Additionally, multidisciplinary models often combine analytical and numerical models of varying fidelity to represent different aspects of the system, which may omit important system dynamics due to inconsistent assumptions across model domains. Identifying and addressing these model limitations requires empirical testing through physical prototyping [28,29].

While hydrodynamic models are typically developed for full-scale WECs, constructing full-scale prototypes at this stage is prohibitively expensive [30,31]. Small-scale prototyping offers a cost-effective alternative that captures essential system physics with significantly reduced material and financial investment. Through the design, fabrication, and testing of scaled WEC devices, researchers gain valuable insights that inform the development of full-scale and pilot-scale systems[32]—enabling better performance and reducing the risk and cost of scaling up [33,34].

Menold et al. [35] presented a "Prototype for X" framework to guide designers from planning to production. They establish key prototyping steps as framing, building, testing, analyzing, and iterating. Our work develops a methodology for the framing, building, and testing WEC prototypes, specifically highlighting relevant couplings and sub-iterations within each step. Camburn and Wood [36] developed principles for do-it-yourself prototyping. This is extremely relevant to the cost-minimization required in WEC prototyping. The principles of repurposing and standardization were crucial in the development of our prototypes; however, these heuristics are not emphasized in our methodology. Lauff collaborated with Menold and Wood [37] to develop their Prototyping Canvas, a tool for designers to focus their prototyping endeavors. They underscore the criticality of assigning purpose to a prototyping project. We emphasize this in our design considerations, urging designers to define clear project goals that align with available resources.

1.3 WEC Prototyping Considerations.

Several key analyses must be conducted before designing and fabricating WEC prototypes to ensure they accurately reflect the physics of the full-scale system. A primary concern is defining the appropriate fluid regime, which is dictated by the testing facility's limits on water depth, wave height, and wave frequency. These parameters determine whether the system operates in shallow, intermediate, or deep water, and each regime influences wave behavior, hydrodynamic forces, and model scaling laws.

Accurately matching the fluid regime between experiment and model is essential for dynamic similarity. A prototype tested under one regime cannot be expected to validate a model intended for another without appropriate correction. These distinctions are frequently underappreciated in small-scale WEC research, leading to model–experiment mismatches.

Additional considerations include material selection, matching the device's natural frequency to the wave spectrum, PTO subsystem design, motor selection, gear ratio specification, structural failure analysis, mooring strategies, electronics integration, and data monitoring and control software development. Each of these topics is addressed in detail in the following section.

This article details the design and manufacturing of two small scale WEC prototypes developed for deep-water WEC array testing. This work includes the construction of four heaving PAs, four OSWECs, two PTOs (commonly referred to as powertrains), mooring components, an integrated electronics system, and dedicated forced-oscillation and control software. Detailed analyses, design rationales, and full documentation of materials and machining processes are provided. All code and CAD drawings used in this study are available in a Github repository, available at the SEA Lab WEC Prototyping Github. The aim is to offer a practical guide for researchers building small-scale WECs, while also supplying essential context for the experimental results available at [38].

2 Analysis

2.1 Overarching Design Considerations.

Before initiating prototype development, it is essential to establish both the experimental objectives and the physical constraints of testing. Among these, the choice of testing facility is the most critical, as its capabilities define the fundamental limits of the study. Determining the scope of experimental goals and selecting an appropriate test facility can be an iterative process, as certain research questions may not be answerable given facility constraints. An overview of these overarching considerations is provided in Fig. 2. In this design flowchart, the project goals and testing facility are grouped together and iterable. Once those two aspects are solidified, the fluid regime, scaling method, and modeling scheme can be developed and analyzed. Further details on each analysis block are provided in the following subsections.

Accepted Manuscript Not Copyedited

Downloaded from http://asmedigitalcollection.asme.org/mechanicaldesign/article-pdf/doi/10.1115/1.4070757/7582635/md-25-1640.pdf by guest on 05 January 2026

Journal of Mechanical Design. Received September 05, 2025;
Accepted manuscript posted January 5, 2026. doi:10.1115/1.4070757
Copyright © 2026 by ASME; reuse license CC-BY 4.0

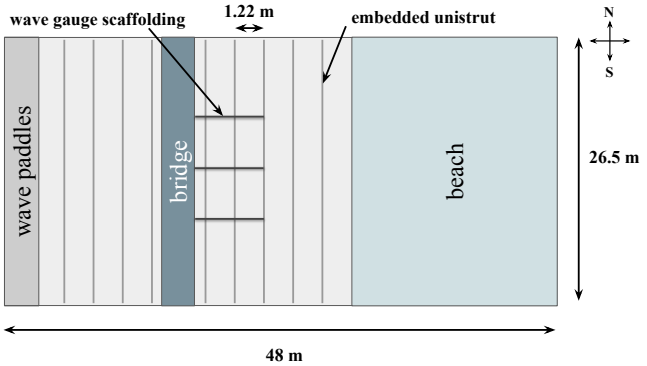

Fig. 3 Diagram of the O.H. Hinsdale Directional Wave Basin.

2.1.1 Testing Facility. Before defining any requirements, the test facility must first be determined. For the prototypes detailed in this paper, the targeted test location was the O.H. Hinsdale Directional Wave Basin at Oregon State University. The basin is equipped with above-water scaffolding that supports an array of wave gauges. It features wave paddles capable of generating both multidirectional and random waves. Based on guidance from the facility supervisor, wave frequencies exceeding 1 Hz (1 s period) were not recommended for testing. A schematic of the basin, including key dimensions, is provided in Fig. 3.

2.1.2 Fluid Regime. The experimental fluid regime has significant implications for both device design and data interpretation. In this study, deep water assumptions were maintained to avoid complexities in Froude scaling laws (Section 2.1.3), as the similitude parameters for Froude scaling become more complicated in intermediate and shallow water regimes. Additionally, breaking waves were avoided, as their strong nonlinearities were beyond the scope of this investigation.

To remain within the desired fluid regime, the following conditions were satisfied (see Fig. 4):

Fluid R1. The ratio of water depth to wavelength must be greater than or equal to 0.5; $\left(\frac{h}{L} \geq 0.5\right)$.

Fluid R2. The ratio of wave height to wave length must be less than $0.142\tanh(kh)$; $\left(\frac{H}{L} < 0.142\tanh(kh)\right)$.

At our testing facility, the maximum permissible water depth was 137 cm. This constraint limited the test environment to wave heights ranging from 1 to 10 cm and wavelengths between 156 cm (corresponding to a 1.0 s wave period) and 274 cm (corresponding to a 1.33 s wave period). It should be noted that a few experiments fell in the intermediate fluid regime. The expected water depth was 20 cm deeper than the actual achievable depth, and experiments with a wave period of 1.39 s were conducted. Once this discrepancy was realized, the experiments were redone at the 1.33 s wave period for deep water evaluation. A specific deployment location was not considered for these experiments, as the focus was experimental validation. This limits the contexts to which the results can be applied. However, the tested wave periods range from 7.07 s to 9.40 s at full ocean-scale. These wave periods are commonly found in real wave spectra, allowing broader applications of the results to real ocean scenarios.

2.1.3 Froude Scaling. Ocean deployments are costly, and testing a full-scale WEC is generally infeasible in most testing facilities. Therefore, devices must be scaled down to fit within the physical constraints of test tanks and basins. In fluid dynamics, several scaling approaches exist, such as Reynolds, Weber, and Froude scaling [40], each based on different dominant forces. However,

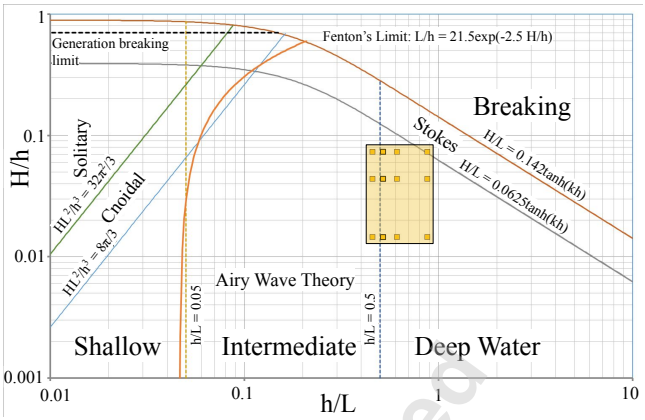

Fig. 4 Chart to identify operating fluid regime based on the ratio of wave height (H) to water depth (h) and water depth to wavelength (L). The yellow squares indicate where our experiments fell. Image provided for this project by [39].

it is often impractical or impossible to simultaneously match all relevant dimensionless numbers. As a result, the scaling method is typically selected based on the dominant physical effects and the assumptions of the model. For this study, Froude scaling was selected as it assumes gravitational forces dominate over viscous forces. This assumption aligns with our model (see Section 2.1.4) and is commonly used in WEC experimentation [41,42].

The Froude number is the ratio between inertial forces and gravitational forces in ocean wave fluid dynamics [40] and is given by

$$Fr = \sqrt{\frac{\text{inertial forces}}{\text{gravitational forces}}} = \sqrt{\frac{\rho L^2 V^2}{\rho L^3 g}} = \frac{V}{\sqrt{gL}}, \tag{1}$$

where V is the fluid velocity [m/s], g is the acceleration due to gravity [m/s^2], and L is the wavelength of the gravitational waves [m]. The Froude number of the prototype (p) must be equal to the Froude number at full-scale (f):

$$Fr_p = Fr_f \Rightarrow \left(\frac{V}{\sqrt{gL}}\right)_p = \left(\frac{V}{\sqrt{gL}}\right)_f. \tag{2}$$

The scaling factor, λ, is defined as the ratio of prototype characteristic wavelength to the full-scale wavelength, given as

$$\lambda = \frac{L_p}{L_f}. \tag{3}$$

This value defines all the similitude parameters of the Froude law. The scale factors for each relevant parameter are shown in Table 1. The prototypes described in this paper were built at a 1:50 scale ($\lambda = 0.02$). This size was chosen due to machining capabilities, initial wave flume size (for preliminary tests), and ability to maintain deep water assumptions.

Table 1 Froude scale factors for relevant dimensions.

Variable	Dimension	Scale factor
Length	[m]	λ
Time	[s]	$\sqrt{\lambda}$
Force	[N]	λ^3
Structural Mass	[kg]	λ^3
Pressure	[Pa]	λ
Moment	[N-m]	λ^4

Accepted Manuscript Not Copyedited

Downloaded from http://asmedigitalcollection.asme.org/mechanicaldesign/article-pdf/doi/10.1115/1.4070757/7582635/md-25-1640.pdf by guest on 05 January 2026

Journal of Mechanical Design. Received September 05, 2025;
Accepted manuscript posted January 5, 2026. doi:10.1115/1.4070757
Copyright © 2026 by ASME; reuse license CC-BY 4.0

An important scaling consideration for the presented prototypes was the following requirement: *Geom R1. The PA and OSWEC prototypes must remain at the same scale* (i.e., $\lambda_{PA} = \lambda_{OSWEC}$). This requirement was unique to this study, as the two WEC architectures were to be tested simultaneously, imposing constraints on the analysis presented in Section 2.2.3.

2.1.4 Numerical Model. To inform the design and testing of physical WEC prototypes, numerical simulations were used to develop initial hypotheses and gain insight into expected system behavior. Among the various modeling approaches available, the Boundary Element Method (BEM) was selected due to its balance between computational efficiency and predictive capability.

BEM simulations compute hydrodynamic coefficients for a meshed geometry with defined hydrostatic properties. These hydrodynamic coefficients are used to compute the expected device dynamics and mechanical power production to inform design requirements for the physical prototype. The coefficients are computed in the frequency domain under linear potential flow assumptions (inviscid, irrotational, incompressible). These assumptions significantly reduce computation time compared to full computational fluid dynamics (CFD), but at the cost of neglecting viscous effects.

Despite this limitation, inviscid numerical models like BEM offer valuable insight into system dynamics and serve as a foundation for higher fidelity studies. Moreover, empirical corrections, such as the inclusion of viscous drag terms, can be incorporated to improve accuracy without sacrificing computation time [43–45]. These corrections are often informed by physical experiments, further motivating prototype development. In this study, simulations were performed using Capytaine [46], an open-source implementation of the BEM solver NEMOH [47].

2.2 Mechanical Design. The mechanical design methodology is summarized in Fig. 5. In this design flowchart, the device geometry and powertrain design are coupled as the powertrain dynamics affect the WEC float dynamics. Once the geometric, hydrostatic, and hydrodynamic aspects of the mechanical WEC system have been determined, the mooring, experimental requirements, and structural failure can be addressed. Each block is described in depth in the following subsections.

2.2.1 Overview of Designs. Before presenting the analyses of the physical prototypes, we provide an overview of the final designs.

The final PA design (physical prototype and its CAD rendering are shown in Fig. 6) consisted of a cylindrical float of marine foam sandwiched between two 1/2" (12.7 mm) thick aluminum disks. The float was machined with three through-holes fitted with linear motion bearings, enabling oscillation along three vertical shafts. These shafts were secured to a top plate, which supported the motor housing, and to a bottom plate, which attached to the mooring structure. A bridge was bolted to the top of the float to hold a rack, which meshed with a pinion in the powertrain to drive the motor.

The final OSWEC design (final physical prototype and CAD model are shown in Fig. 7) featured a marine-foam float sandwiched between two acrylic sheets, held together by aluminum struts through which a shaft was threaded. One of the struts also supported a curved rack for power transmission. An aluminum bar was mounted at the bottom of the float. Shaft collars on either side secured the float, while mounted bearings bolted to the mooring structure and allowed the flap to rotate freely. An overhead bridge supported the motor housing.

2.2.2 Device Dynamics and Power Production. In WEC design, the device motion is commonly characterized by the response amplitude operator (RAO), defined as the ratio of the magnitude of the complex body motion ($\mathbb{X}_i$) to the incident wave amplitude (A) [48]:

$$RAO = \frac{|\mathbb{X}_i|}{A}. \tag{4}$$

The complex body motion is given by

$$\mathbb{X}_i = \frac{\mathbb{F}_i}{\sum_j \left(-\omega^2(I_{ij} + A_{ij}) + i\omega B_{tot} + K_{tot}\right)}, \tag{5}$$

where $\mathbb{F}_i$ is the complex wave excitation force or torque [N or N-m], ω is the wave frequency [rad/s], I_{ij} is the inertia or mass matrix [kg and kg-m^2], A_{ij} is the added mass matrix [kg and kg-m^2], B_{tot} is the total damping matrix [kg/s and kg-m^2/s], and K_{tot} is the total stiffness matrix [kg/s^2 and kg-m^2/s^2]. The subscripts i and j denote the degree of freedom (1-6).

The stiffness term expands to

$$K_{tot} = K_{ij} + K_{PTO}, \tag{6}$$

where K_{ij} is the hydrostatic stiffness matrix and K_{PTO} is additional stiffness provided by the PTO.

The damping term expands to

$$B_{tot} = B_{ij} + B_{PTO} + B_{viscous}, \tag{7}$$

where B_{ij} is the radiation damping matrix, B_{PTO} is damping provided by the PTO, and $B_{viscous}$ is the linearized viscous damping coefficient [49]

$$B_{viscous} = \gamma_{nl}\frac{8\omega RAO}{3\pi}, \tag{8}$$

where γ_{nl} is a nonlinear drag term estimated from literature. The PTO coefficients were implemented in the control software and for power estimation, but excluded from initial hydrodynamic design calculations.

Viscous damping was expected to significantly impact the OSWEC flap motion [50] and was included in its motion model. Experimental results showed that viscous damping did impact the PA device motion, however, in a manner that did not follow the traditional viscous damping trend ([51] in prep). An empirical fit was required to model this damping, which was likely attributable to viscous friction in the linear sleeve bearings.

Mechanical power production (P_{mech}) is typically of interest during WEC experimentation. The following form was used to estimate mechanical power production:

$$P_{mech} = \frac{1}{2}B_{PTO}|\dot{\mathbb{X}}_i|^2. \tag{9}$$

Defining the expected mechanical power production is necessary to quantify structural requirements in the PTO. Additionally, if an electrical power production system is included, the mechanical power is necessary to define the electronics requirements.

2.2.3 Geometric and Hydrostatic Properties. The geometric and hydrostatic parameters of a WEC device are chosen to achieve a specific hydrodynamic response. If the desired project outcome is maximum mechanical power production, the magnitude and phase of the complex body velocity should be optimized (see Eq. 9). The optimal power production P_{opt} is expressed by Falnes [52] as

$$P_{opt} = P_{MAX}\cos^2(\gamma_i), \tag{10}$$

where γ_i is the phase angle between the device motion and wave excitation force and P_{MAX} is the maximum power, which occurs at $\gamma_i = 0$. In passive control, this becomes

$$\cos^2\gamma_i = \frac{1}{1 + c^2\left[\left(\frac{\omega}{\omega_n}\right)^2 - 1\right]^2}, \tag{11}$$

Not Copyedited Manuscript

Downloaded from http://asmedigitalcollection.asme.org/mechanicaldesign/article-pdf/doi/10.1115/1.4070757/7582635/md-25-1640.pdf by guest on 05 January 2026

Journal of Mechanical Design. Received September 05, 2025;
Accepted manuscript posted January 5, 2026. doi:10.1115/1.4070757
Copyright © 2026 by ASME; reuse license CC-BY 4.0

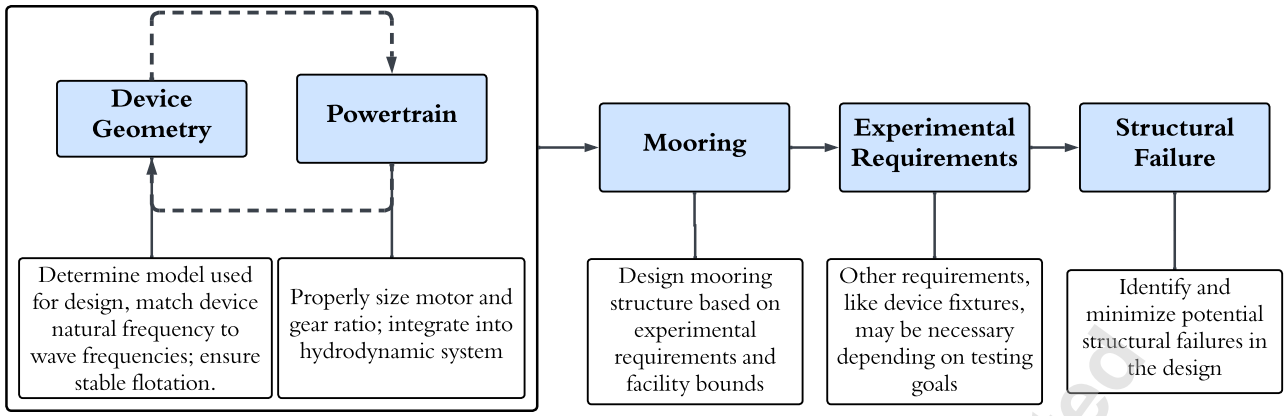

Fig. 5 Mechanical design methodology flowchart.

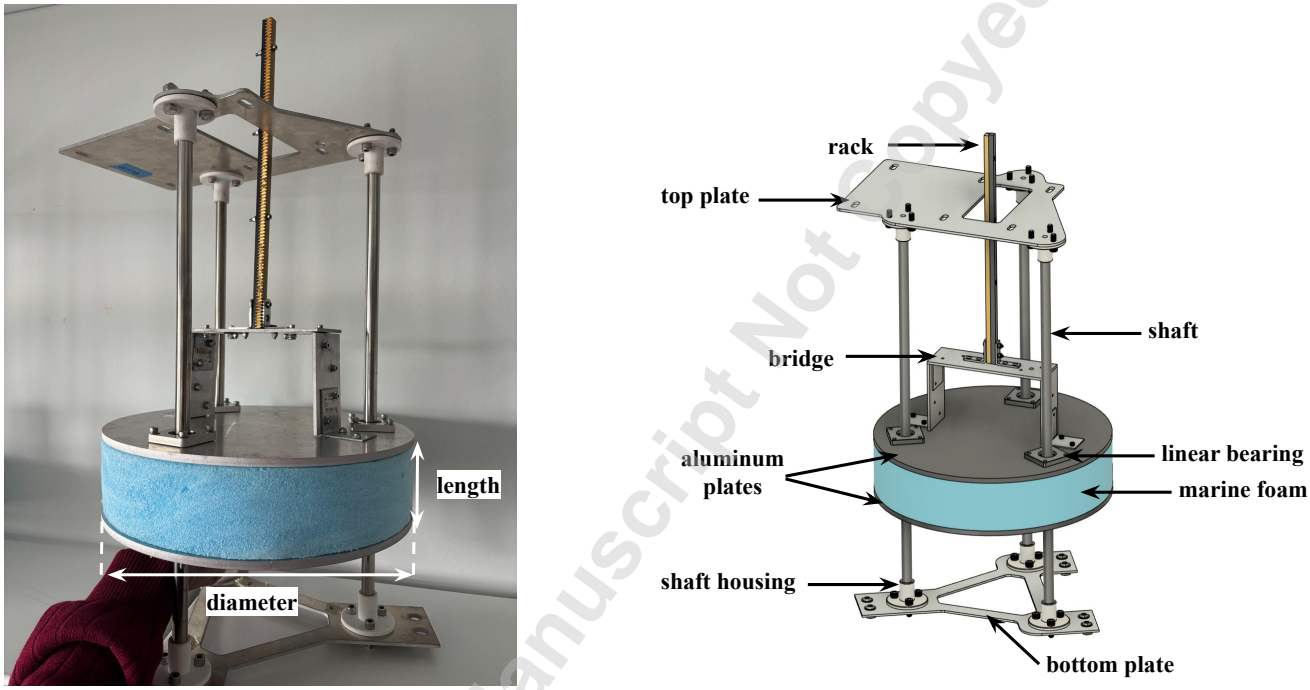

(*a*) (*b*)

Fig. 6 Final mechanical design of heaving PA (a) physical prototype with referenceable dimensions and (b) CAD rendering with labeled components.

where $c = K_{ij}/(\omega B_{tot})$, and we see that hydrodynamic resonance ($\omega = \omega_n$) maximizes power. In the case without mechanical power production, we can represent the RAO as

$$RAO = \frac{\mathbb{F}_i}{A\omega(B_{ij} + B_{viscous})\sqrt{1 + c^2\left[\left(\frac{\omega}{\omega_n}\right)^2 - 1\right]^2}} \tag{12}$$

where $c = K_{ij}/(\omega(B_{ij}+B_{viscous}))$, and we see that hydrodynamic resonance maximizes the uncontrolled response amplitude as well. Therefore, the WEC device should be designed with a natural frequency that matches the wave frequencies it will experience during deployment. The desired fluid regime and tank capabilities limited the testable wave frequencies. This introduced the following requirement: *Geom R2. The devices must be designed for a natural frequency of oscillation that approaches the experimental wave frequency range.* The device's accelerating mass, float dimensions, center of mass, and center of buoyancy required adjustment to satisfy this requirement. PTO impedance was not accounted for when designing for a specific natural frequency, as the main focus of this study was the device's hydrodynamic response.

Point Absorber. It was challenging to hydrodynamically approach the ideal natural frequency for the PA. Due to the nature of PA geometries, their stiffness in heave is high, resulting in designs that exhibit a higher natural frequency than their targeted wave spectra. To determine the achievable natural period (T_n) of the PA float, an analytical model was derived for faster computation in the first pass analysis. The desired float draft was set to 75% of the float length (l), and the accelerating mass of the PA (m_{PA}) was determined based on the mass of the volume of displaced water, shown as

$$m_{PA} = \frac{3}{4} l \rho_w \pi r^2, \tag{13}$$

Accepted Manuscript Not Copyedited

Downloaded from http://asmedigitalcollection.asme.org/mechanicaldesign/article-pdf/doi/10.1115/1.4070757/7582635/md-25-1640.pdf by guest on 05 January 2026

Journal of Mechanical Design. Received September 05, 2025;
Accepted manuscript posted January 5, 2026. doi:10.1115/1.4070757
Copyright © 2026 by ASME; reuse license CC-BY 4.0

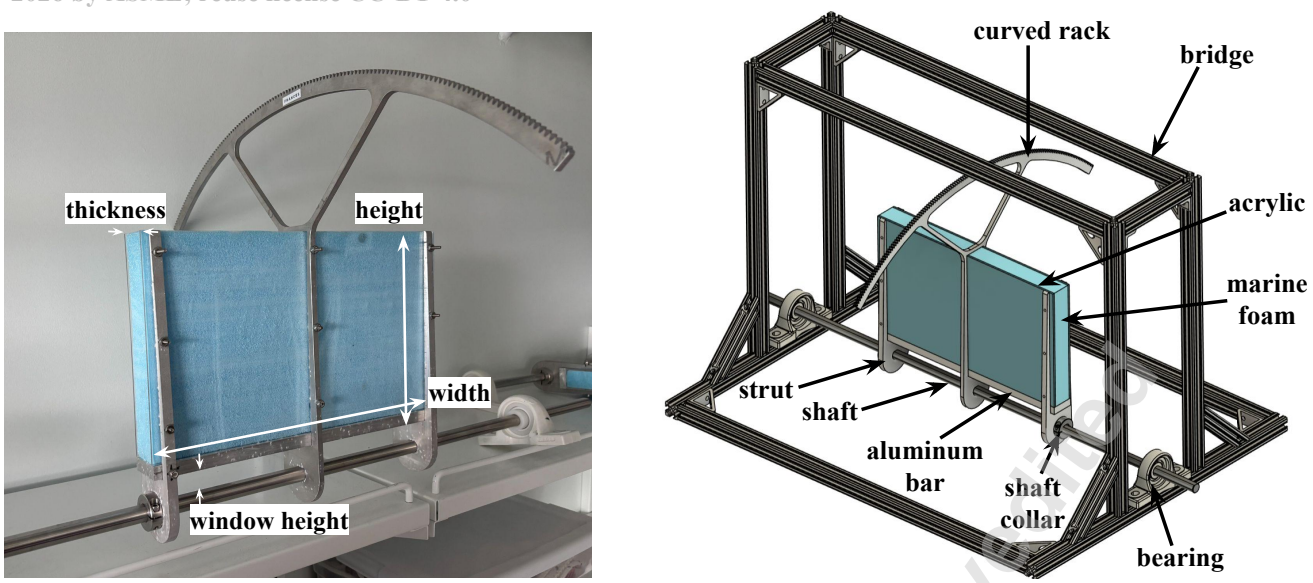

Fig. 7 Final mechanical design of OSWEC (a) physical prototype with referenceable dimensions and (b) CAD rendering with labeled components.

where ρ_w is the density of water [kg/m^3] and r is the radius of the float [m]. The water plane area ($A_{wp} = \pi r^2$) was computed in order to find the hydrostatic stiffness, which Falnes [52] defines as

$$K_{33} = \rho_w g A_{wp}. \tag{14}$$

Next, the added mass in heave (A_{33}) was approximated in 3D using [53], and is equivalent to the PA mass approximation

$$A_{33} = m_{PA}. \tag{15}$$

Analytical approximations of added mass are low fidelity. This was done as the first pass analysis for computational speed and gaining intuition about system behavior with respect to the design variables (l and r). Finally, the natural frequency (ω_n) can be found by

$$\omega_n = \sqrt{\frac{K_{33}}{m_{PA} + A_{33}(\omega)}} \tag{16}$$

and the natural period as

$$T_n = \frac{2\pi}{\omega_n}. \tag{17}$$

The bridge and rack masses were set and were subtracted from the full PA mass to find the required mass of only the float. The results of this analysis are seen in Fig. 8. In the presented analytical formulation, radius bears no effect on the natural period of the device, solely on the mass. The higher-fidelity numerical analysis showed dependence on radius, with larger radii resulting in longer natural periods. Increasing the length of the float also produced a longer natural period. However, manufacturing capabilities limited the final float dimensions. With our capabilities and timeline, the maximum float diameter was restricted to 0.2921 m and the float length to 0.0889 m.

Therefore, the final design featured the maximum possible float length (0.0889 m) and diameter (0.2921 m). This corresponded to a natural period of approximately 0.7326 s and a goal float mass of 4.131 kg. These dimensions and draft were then meshed and evaluated in Capytaine for more accurate added mass calculations. The total mass of the final physical prototype (m_{PA} = 3.462 kg) was used for the final numerical predictions. The expected natural period of the device was 0.6937 s. The dimensions and hydrodynamic properties of the final PA float design are summarized in Table 2.

Table 2 Dimensions and hydrodynamic properties of final float design.

Parameter	Value	Units
Length	0.0889	[m]
Diameter	0.2921	[m]
m_{PA}	3.462	[kg]
A_{33}	5.58 to 6.73	[kg]
K_{33}	654	[kg/s^2]
T_n	0.6937	[s]
c_b (from top of float)	0.0258	[m]
c_g (from top of float)	0.0647	[m]

The experimentally determined natural period of the PA prototype was between 0.70 and 0.72 s. The analytical approximation had between 1.75% and 4.7% error, whereas the BEM model error ranged from 0.9% and 3.7% error. The analytical method did an adequate job predicting natural period, and the BEM model only slightly improved the prediction.

The natural period of the PA was outside of the testing range (1.0 s to 1.39 s), resulting in a suboptimal design. The hydrodynamic resonance requirement (Geom R2) was enforced late in our design process, and we recommend introducing it earlier to mitigate manufacturability limitations.

OSWEC. The OSWEC needed to approach the desired natural frequency and maintain stable flotation. The curved rack was not part of the original float design. The rack significantly altered the center of mass and the mass moment of inertia of the float, requiring significant design alterations. The following requirements were imposed:

OS R1. The OSWEC's equilibrium position must be vertical, with 90° between the water surface and the flap edge.

Accepted Manuscript Not Copyedited

Downloaded from http://asmedigitalcollection.asme.org/mechanicaldesign/article-pdf/doi/10.1115/1.4070757/7582635/md-25-1640.pdf by guest on 05 January 2026

Journal of Mechanical Design. Received September 05, 2025;
Accepted manuscript posted January 5, 2026. doi:10.1115/1.4070757
Copyright © 2026 by ASME; reuse license CC-BY 4.0

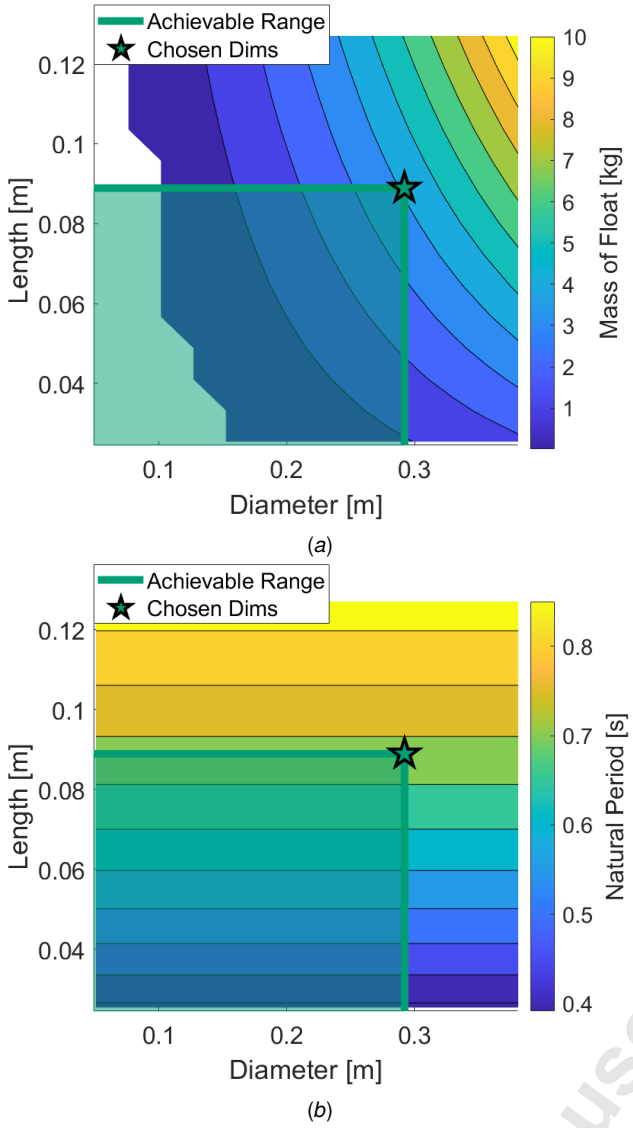

Fig. 8 a. Depicts the float mass with respect to the length and radius of the float (keeping the draft constant), b. Depicts the natural period with respect to the length and radius of the float.

OS R2. The rack gear teeth must be manufacturable using a waterjet.

OS R3. The angular span of the rack must accommodate the device's expected operating angle (ϕ).

OS R4. The rack radius must be large enough such that the motor subassembly remains out of the water.

These requirements ensured that the rack would successfully act in the PTO, the float would remain stable, and the rack would be machinable, all while tuning the natural period of the device.

To satisfy the first requirement, the center of mass needed to be below the metacentric height, requiring tuning of the thickness, width, and draft. The mass of the rack was reduced and significant mass was added to the bottom of the flap.

The initial curved rack design used 3/8" (9.525 mm) thick 6061 aluminum to ensure stiffness for gear meshing. This first pass design served as a proof of concept and identified high priority areas for design improvement. The gear tooth size and geometry was chosen as a standard 20 degree pitch angle 1.5 module metric gear. The 1.5 module ensured the gear teeth would be large enough to be accurately machined with a waterjet, satisfying the second requirement. The angular span of the rack was determined based on BEM simulations, which predicted a maximum operating angle of 20 degrees, satisfying the third requirement. The motor subassembly had a 7.5 cm radius, the flap height was 21.6 cm, and the highest wave amplitude tested was 10 cm. This set the required rack radius to 39 cm, satisfying the fourth requirement.

The device motion follows the form in Eq. 5. The hydrostatic stiffness in pitch (K_{55}) is the result of the torques due to buoyancy and gravity about the hinge, resulting in

$$K_{55} = \rho_w V_{sub} g c_b - m_{tot} g c_g, \tag{18}$$

where V_{sub} is the submerged volume of the flap [m^3], c_b is the location of the center of buoyancy [m], m_{tot} is the total mass of the flap and curved rack [kg], and c_g is the center of gravity of the combined flap and rack [m]. The natural frequency is defined similarly to Eq. 16

$$\omega_n = \sqrt{\frac{K_{55}}{I_{55} + A_{55}(\omega)}}. \tag{19}$$

The angular motion of the flap was linearized using the small angle approximation, $\sin(\theta) \approx \theta$. This approximation avoids nonlinear terms in the buoyancy and gravitational torques. Under the assumption that the maximum flap angular displacement is about 20°, this is a good approximation.

The curved rack underwent a series of simulated design iterations to reduce rotational inertia, thereby increasing the natural frequency. The rack thickness was reduced to 1/4" (6.35 mm), and the supports for the rack were decreased from four to two trusses. The radius was kept constant at 39 cm. The final properties of the new curved rack design included a mass of 0.297 kg, a center of mass at 0.234 m, and a moment of inertia at the origin of 0.0262 kg-m^2. However, solely changing the rack design was insufficient to reach the desired natural frequency range and center of mass.

In the final design, the thickness of the marine foam was increased by 25%, the window height of flap was increased by 1.0 cm, the flap height was increased, and the draft was decreased to 85% of the flap height. Additionally, a solid 1/2" (1.27 cm) thick aluminum bar was added to the base of the flap, adding mass towards the axis of rotation and lowering the center of gravity. The culmination of these design changes approached the desired natural period range, with the expected value of 2.045 s. However, like the PA, the OSWEC did not fall precisely within the testing range. The dimensions and hydrodynamic properties of the final flap design are summarized in Table 3.

Table 3 Properties of final flap design.

Parameter	Value	Units
Width	0.36	[m]
Height	0.216	[m]
Thickness	0.0381	[m]
Window height	0.0282	[m]
Mass	1.625	[kg]
I_{55}	0.0405	[kg-m^2]
A_{55}	0.092 to 0.117	[kg-m^2]
K_{55}	1.153	[kg-m^2/s^2]
T_n	2.045	[s]
Draft	0.184	[m]
c_g (from top of flap)	0.1338	[m]
c_b (from rotating shaft)	0.1219	[m]

The OSWEC's natural period found from experimentation was between 2.893 s and 3.163 s. The error in the numerical model's

Accepted Manuscript Not Copyedited

Downloaded from http://asmedigitalcollection.asme.org/mechanicaldesign/article-pdf/doi/10.1115/1.4070757/7582635/md-25-1640.pdf by guest on 05 January 2026

Journal of Mechanical Design. Received September 05, 2025;
Accepted manuscript posted January 5, 2026. doi:10.1115/1.4070757
Copyright © 2026 by ASME; reuse license CC-BY 4.0

natural period prediction was between 29.3% and 35.3%. There are several potential causes for this discrepancy, such as the centers of gravity and buoyancy of the physical prototype not precisely matching the model. However, it is likely due to out-of-phase drag force that manifests as a stiffness rather than a damping, since the OSWEC experiences significant drag [45].

As aforementioned, it is recommended to incorporate Geom R2 before any design parameters are set. This allows more design freedom and a higher likelihood of achieving the desired natural period of oscillation.

2.2.4 Powertrain. The powertrain mechanism for a small-scale WEC prototype should: *PTO R1. minimize friction to maintain linearity and avoid locking.* This is crucial for small-scale WEC prototypes, as the relatively small wave excitation loads can be the same order of magnitude as friction in the system. Additionally, the gear ratio of the PTO is critical for maintaining sufficient device operation, and it can be tuned to achieve desired dynamics. WECs move at a low speed with high inertia, but motors prefer to operate at high speeds with low torque. This produced the following requirements:

PTO R2. The PTO pinion must be large enough to provide enough torque to overcome friction in the powertrain (low gear ratio).

PTO R3. The PTO pinion should be as small as possible (within the above constraint) such that the motor will spin faster than the WEC motion (high gear ratio).

PTO R4. The motor must maintain amplitudes of current and angular velocity that are detectable by sensors for both control and logging.

Ultimately, the device gear ratios were determined through a guess-and-check method. Initial guesses were based on test-gears made out of acrylic and machined in a lasercutter. This allowed preliminary testing of different gear ratios before purchasing more expensive, robust gears.

The large curved rack on the OSWEC (39 cm radius, 520 teeth) was extremely effective at the small-scale. With this large rack design, a gear ratio of 14.4 was achieved, allowing the device to easily overcome friction in the powertrain with a relatively small PTO pinion (2.7 cm pitch radius, 36 teeth). Using a small PTO pinion allowed the motor subassembly to remain compact, readily integrating with the mechanical system.

The PA was limited to a much higher gear ratio of 25 mm/rad. This gear ratio is dimensional due to the straight rack creating a ratio between translation velocity and rotational velocity. This was the largest pinion able to integrate into the existing PA powertrain. Because of this limitation, the PAs struggled to overcome friction in the PTO at certain incident wave frequencies and amplitudes. The devices functioned adequately, but a lower gear ratio would have improved their performance.

Earlier in the design process, simulations were run in attempt to approximate acceptable gear ratios. However, this requires accurately quantifying the static and dynamic friction in the powertrain. We were not able to precisely quantify this friction, leading to the guess-and-check method. The mathematical formulation is found in Appendix A, and would be useful if the powertrain friction is known.

The following section details requirements for selecting a motor, but it should be noted that the analysis of gear ratio and the motor is iterative. Simultaneous evaluation is necessary to fulfill PTO R1-4 and Motor R3-5.

2.2.5 Motor Selection. A motor, or other mechanism for converting mechanical power to electrical power, should be integrated into the mechanical system if electrical power production is required. The motor used in the PTO should be sized based on the expected power output of the WEC device (see Section 2.2.2). The key requirements for determining an appropriate motor are:

Motor R1. Peak power output is greater than device maximum power output (700 W)

Motor R2. Continuous power output is greater than device average power output (500 W)

Motor R3. Continuous torque rating is ≥ device average torque (1.4 N-m)

Motor R4. Peak torque is ≥ device max torque (2.43 N-m)

Motor R5. Peak speed is ≥ device max angular speed (2750 RPM)

where the values in parentheses correspond to the power and applied torque values initially estimated for the devices in this report. After evaluating several motors, the CubeMars R80 Brushless DC Outrunner Motor was chosen. It is rated for a continuous torque of 1.3 N-m, a peak torque of 4 N-m, continuous torque max speed of 4600 RPM, a continuous current rating of 15 A, a peak current of 46 A, and a voltage rating of 48 V. This meets every design requirement listed above. Additionally, this motor has a lead time of only seven days, accelerating the development of the prototypes.

Early simulations predicted power outputs on the order of hundreds of W. This was a severe overestimate and resulted in an over-sized motor. The actual expected power output for the final devices was on the order of mW. Additionally, several practical challenges arose during fabrication and operation that should be incorporated into motor selection requirements:

Motor R6. The motor must introduce minimal additional friction to the powertrain.

Motor R7. The motor must be selected such that integration with the rest of the powertrain is straightforward.

Motor R8. The motor must be able to respond to control commands with an accuracy, precision, and bandwidth defined by project goals.

2.2.6 Motor Subassembly. The main design considerations for the motor subassembly were rigidity, adaptability, and water resistance. The summary of functional requirements for the motor subassembly are:

PTO R5. The motor housing must remain rigid throughout experimentation.

PTO R6. The pinion in the powertrain must mesh with the rack on the device.

PTO R7. One side of the motor must be rigidly fixed while the other is free to rotate.

PTO R8. The motor and connecting wires must be protected from water influx.

PTO R9. Rotation of the pinion must result in rotation of the motor.

PTO R10. The PA and OSWEC must use the same motor housing.

The final motor subassembly physical prototype and CAD design are shown in Fig. 9. A torque sensor was mounted between an aluminum plate and the motor. However, securing the sensor directly to the aluminum plate did not provide enough rigidity, and small translational displacements were observed during motor operation. To address this, a custom adapter was manufactured to connect the torque sensor to the motor, but the resulting setup was complex and difficult to assemble. A better approach would have

Accepted Manuscript Not Copyedited

Downloaded from http://asmedigitalcollection.asme.org/mechanicaldesign/article-pdf/doi/10.1115/1.4070757/7582635/md-25-1640.pdf by guest on 05 January 2026

Journal of Mechanical Design. Received September 05, 2025;
Accepted manuscript posted January 5, 2026. doi:10.1115/1.4070757
Copyright © 2026 by ASME; reuse license CC-BY 4.0

been to use a torque sensor and motor that are designed for direct integration, simplifying installation and improving stability. The opposite end of the motor used a custom-made component that connected to the motor and extended into a short shaft. This short shaft was joined to a longer shaft with a shaft collar and passed through a press-fit bearing mounted in a second aluminum plate. However, to improve rigidity in the powertrain, it is recommended to eliminate the shaft collar and replace the two shafts with a single continuous shaft. The two aluminum plates were CNC milled to create an indented circle on their inner wall. These indents allowed an acrylic tube to encase the motor and create a tight fit between the plates. This protected the motor from waves during testing and overfilling of the tank. A small hole was machined into the acrylic tube to allow the hall sensor wires, motor phase wires, and torque sensor wires to be fed through and connect to the electronics system. However, the acrylic tube introduced misalignment in the powertrain because it lacked precision machining. While the acrylic provided good water resistance, using a precut component would have improved alignment.

For the PAs, an additional aluminum plate with a press fit bearing was added to the end of the rotating shaft. This plate held a track roller to ensure the PA rack meshed with the pinion. The original design featured two rollers, but two introduced far too much friction, and one roller was sufficient.

2.2.7 Mooring. The mooring structure requirements were mostly contingent on the O.H. Hinsdale Directional Wave Basin (see Section 2.1.1). A summary of the mooring requirements is as follows:

Moor R1. There must be total freedom in the positioning of the devices in the basin.

Moor R2. The mooring structures must be rigid, as the model validation is focused on specific degrees of freedom.

Moor R3. The mooring structure must not create an artificial floor in order to maintain deep water conditions.

Moor R4. Any generated vortices must have minimal impact on the flow dynamics.

Moor R5. The mooring structures must achieve the desired draft.

To satisfy the first requirement, the devices needed to be bottom moored to the embedded unistrut, as this allowed almost total freedom for placing and spacing the devices. If they were top moored, they would be constricted to the basin's wave gauge scaffolding configuration and overhead bridge. Therefore, the mooring was constructed from t-slotted framing for ease of integration. The framing was made of aluminum to meet strength and corrosion requirements.

Each structure resembled a cage: a box with triangulated pieces of t-slotted framing for support in all directions. This cage structure was rigid and strong, satisfying requirement three. The PAs bottom plate was modified, as the original design used a solid aluminum plate. This solid plate effectively raised the water depth to directly below the PA float, creating a boundary layer and negating the work done to ensure deep water conditions. Instead, a triangular bottom plate was designed, minimizing the amount of material in the bottom plate while providing enough surface area to mount the PA shafts and attach to the t-slotted framing structure. This satisfied the fourth requirement.

The OSWEC's powertrain was designed to be out of the water, requiring a bridge to be constructed above the flap. This bridge attached to the mooring structure and held the motor housing. However, the bridge introduced vortices generated by the vertical t-slotted framing supports. To minimize their influence on the flap, a sufficient distance was required between the vertical framing and the flap's edge. Based on previous experiments, this distance was determined to be five times the thickness of the flap [54]. Additionally, once the devices were in the basin, the central vertical posts were removed, and each OSWEC's motor housing was attached to the same bridge, cutting the number of vertical posts in half. This satisfied the fifth requirement.

The height of the mooring structures was chosen based on the desired OSWEC draft, which is 85% of the device's total height. With an expected water depth of 1.37 m, the mooring height needed to be 1.12 m to achieve this draft. The PA was more flexible, with its limiting factor being the length of the rack-bridge assembly with respect to the expected wave amplitudes. The rack is 30 cm long, raised 8.9 cm above the float by its bridge. This gave an acceptable range of mooring structure heights between 1.0 m and 1.22 m. For simplicity, the PA mooring structure height was made identical to that of the OSWECs. This satisfied the final mooring requirement. A visualization of the still water line (SWL) with respect to the devices and the dimensions used to determine mooring height are shown in Fig. 10.

The mooring structures were initially secured to the tank floor by "sandwiching" other bars of unistrut through the bottom of the mooring structures and securing them into the embedded unistrut. For additional rigidity, tensioned cables were attached to the top of the mooring structures and fastened into the embedded unistrut. Each device had at least three tensioning cables. The final mooring setup is shown in Fig. 11. However, after changing configurations, it was determined that the tensioned cables alone were sufficient to secure the devices, and the unistrut sandwich was only used for one configuration.

2.2.8 Fixing Devices. Tests such as fixed wave excitation and forced oscillation are necessary for system identification and numerical model validation. These experiments are executed to collect wave excitation force and radiation force data. To complete them, each device must be equipped with a method to completely constrain motion while measuring the desired forces. The following requirements must be fulfilled:

Fix R1. A fixture must be designed to constrain the devices from all movement.

Fix R2. While the devices are fixed, the applied load must be measurable in the device's prescribed degree of freedom.

Fix R3. The load-measuring instrument must be rated to handle the maximum wave excitation force (42.56 N or 10 lbf).

Fix R4. The load-measuring device must be waterproof or integrated into the system at a safe distance from the SWL.

Fix R5. The fixture must be able to be attached or detached in less than ten minutes so as not to not introduce delays in experimentation.

Two methods of fixing the devices were designed to satisfy the requirements. The successful fixture effectively added a linkage to each device, with that linkage being RAS1 S Beam Load Cell. This load cell was rated for 50 lbf (222 N) with an accuracy of ±0.02% and had the ability to be fully submerged underwater. Additionally, this load cell included dedicated software capable of supporting five load cells simultaneously, while maintaining time-synchronized data collection. Integrating the load cells into the mechanical design was different for each WEC architecture. For the PA, holes were machined into the top plate and the bridge. Bolts were fed through these holes and fastened to the threaded load cell. This secured the load cell near the center of the device, parallel to the rack. The OSWEC required t-slotted framing, designed to extend the motor housing bridge. This framing held the load cell horizontally, parallel to the water surface.

It was challenging to place these linkages directly in the center of the devices due to their racks. The off-center linkage would produce a moment due to the distributed loads on the devices. An

Downloaded from http://asmedigitalcollection.asme.org/mechanicaldesign/article-pdf/doi/10.1115/1.4070757/7582635/md-25-1640.pdf by guest on 05 January 2026

Accepted Manuscript Not Copyedited

Journal of Mechanical Design. Received September 05, 2025;
Accepted manuscript posted January 5, 2026. doi:10.1115/1.4070757
Copyright © 2026 by ASME; reuse license CC-BY 4.0

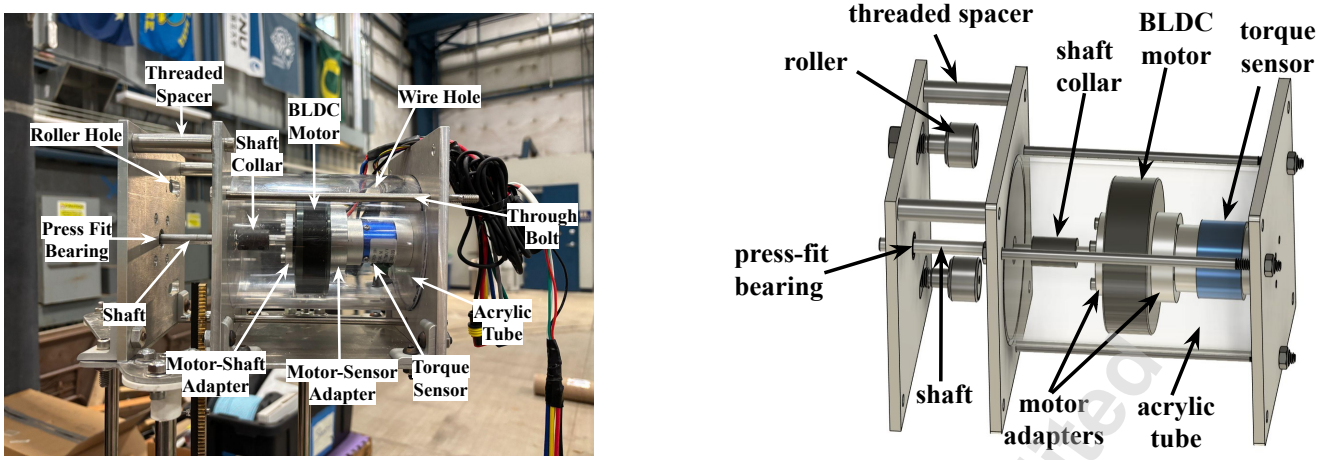

(*a*) (*b*)

Fig. 9 Final mechanical design of motor subassembly (a) physical prototype and (b) CAD rendering.

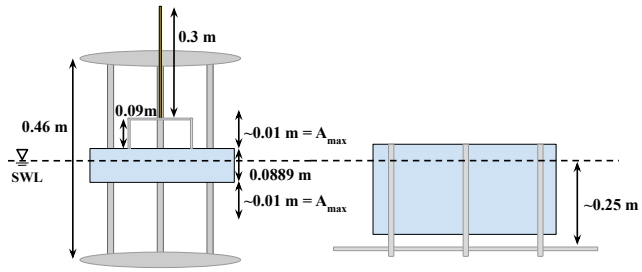

Fig. 10 Depiction of SWL with respect to each device and dimensions used to determine mooring structure height.

experiment quantified the effect of distance from the load cell to the reported measurement, finding a difference of ±0.19% across the moment arm, deeming the effect negligible. Additionally, the load cells were robust and their software incredibly straightforward, making it the preferable option for experimentation. The full depiction of the load cell fixture linkages and the measured loads are shown in Fig. 12.

The alternative design involved fixing the shaft in the PTO and relying on the static torque sensor to measure the resulting forces. This method hinged on the static torque sensor functioning properly. However, the torque sensor used in these designs was not reliable for consistent data acquisition. If a robust sensor was integrated in the powertrain, this method would be preferable, and the design is shown in Fig. 15 in Appendix A.

2.2.9 Minimizing Structural Failure. WEC experimentation can last several weeks, and could potentially span multiple years if the prototypes are reused for several experimental campaigns. Prototypes should be fabricated such that structural failure related to extended lifetimes are quantified and mitigated. The devices in this report had an intended operational lifetime of six weeks. This introduced the following requirements:

FM R1. All components must be designed to withstand cyclic wave loading due to experimentation.

FM R2. All components must be made of corrosion resistant materials that can withstand several weeks of submersion in fresh water.

Bearing and Gear Teeth Loads. A common point of failure in mechanical design is undersized bearings [55]. The point absorber float oscillates along three vertical shafts, each with a linear motion bearing. To ensure the bearings could withstand the full experimental campaign, a bearing load analysis was conducted. Details of this analysis are found in Appendix A. The required load capacity of the bearings for the applied loads was 0.126 N. However, the original expected load capacity was much larger, and flange-mount linear sleeve bearings with a capacity of 1330 N were used. This was 10^5% larger than the required load capacity, and lower load-capacity bearings would be acceptable for most small-scale WEC designs.

Another potential point of failure was gear teeth breakage, especially when the devices are fixed. The Lewis bending stress and Hertzian contact pressure due to the applied loads were analyzed. However, due to the small-scale of experimentation, the applied loads were negligible compared to the material strength of the gears and racks. For example, the expected Lewis bending stress for the PA was 0.004% of the yield stress of its rack and pinion materials. These calculations may be relevant at a larger scale (1:10-1:25), and the mathematical process is included in Appendix A.

Material Selection. The materials used in a long-term wave basin experiment must be corrosion resistant and/or waterproofed. Materials used for these builds included aluminum, stainless steel, acetal, acrylic, polyurethane, and polycarbonate. Additionally, the buoyant element of the device must be carefully considered. These prototypes used marine grade foam with a density of 1 kg/m^3.

All bolts were 18-8 or 303 stainless steel, and the PA shafts were made of 440C stainless steel. The linear bearings in the PAs were made of anodized 6061 aluminum, and every machined part was made with 6061 aluminum stock. The 3D printed parts were manufactured with polylactic acid (PLA), and the mounted shaft bearings for the OSWECs were made of acetal. The PA rack was made of brass. The devices were in the basin for five weeks, and corrosion was not an issue. Structurally, the devices held up well against the wave loading and no damage was observed.

2.3 Electrical Design. An electrical system must be included if the experimental goals require forced oscillation testing and/or electrical power production. Any electrical system introduces the following requirements:

Elec R1. All hardware must operate safely within the voltage and current limits of the motor.

Elec R2. Motor current, motor voltage, motor velocity, and radiation force data must logged with and accuracy and precision

Accepted Manuscript Not Copyedited

Downloaded from http://asmedigitalcollection.asme.org/mechanicaldesign/article-pdf/doi/10.1115/1.4070757/7582635/md-25-1640.pdf by guest on 05 January 2026

Journal of Mechanical Design. Received September 05, 2025;
Accepted manuscript posted January 5, 2026. doi:10.1115/1.4070757
Copyright © 2026 by ASME; reuse license CC-BY 4.0

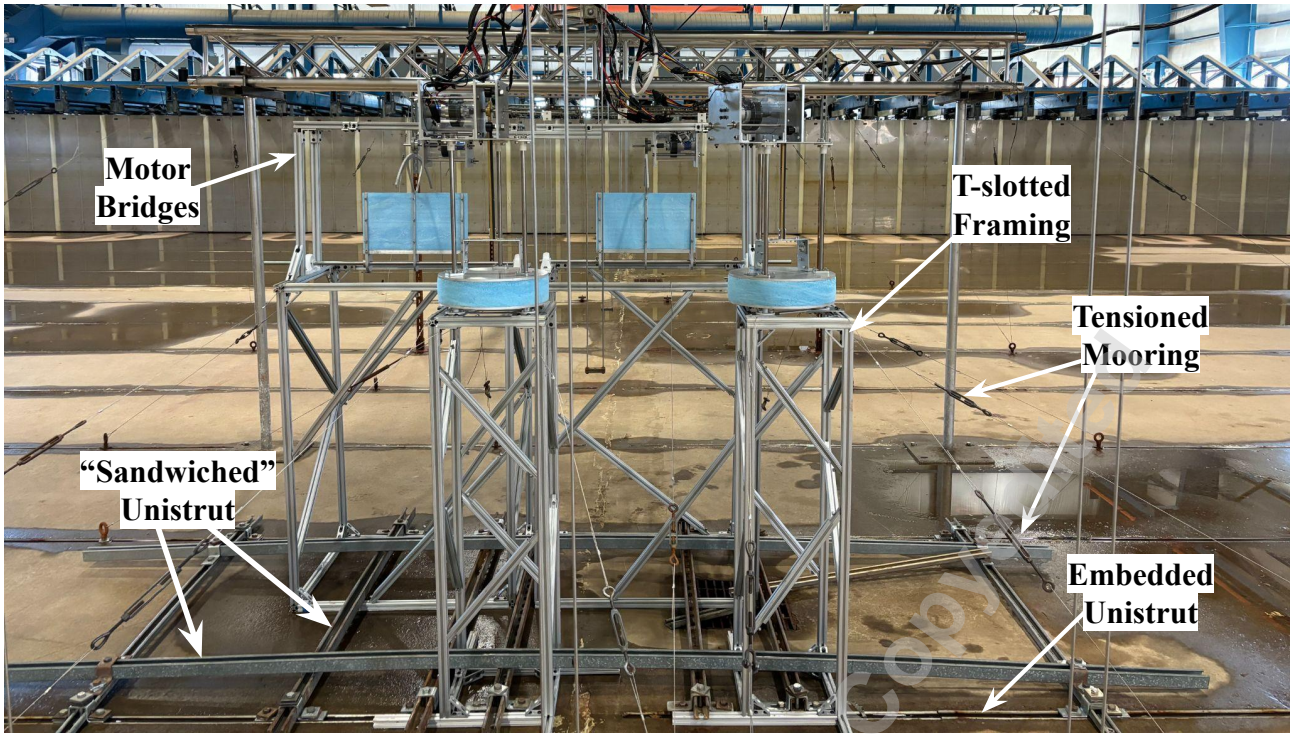

Fig. 11 Mooring setup in the basin for one configuration. The unistrut sandwich, tensioned mooring lines, t-slotted frames, and the motor housing bridges are labeled.

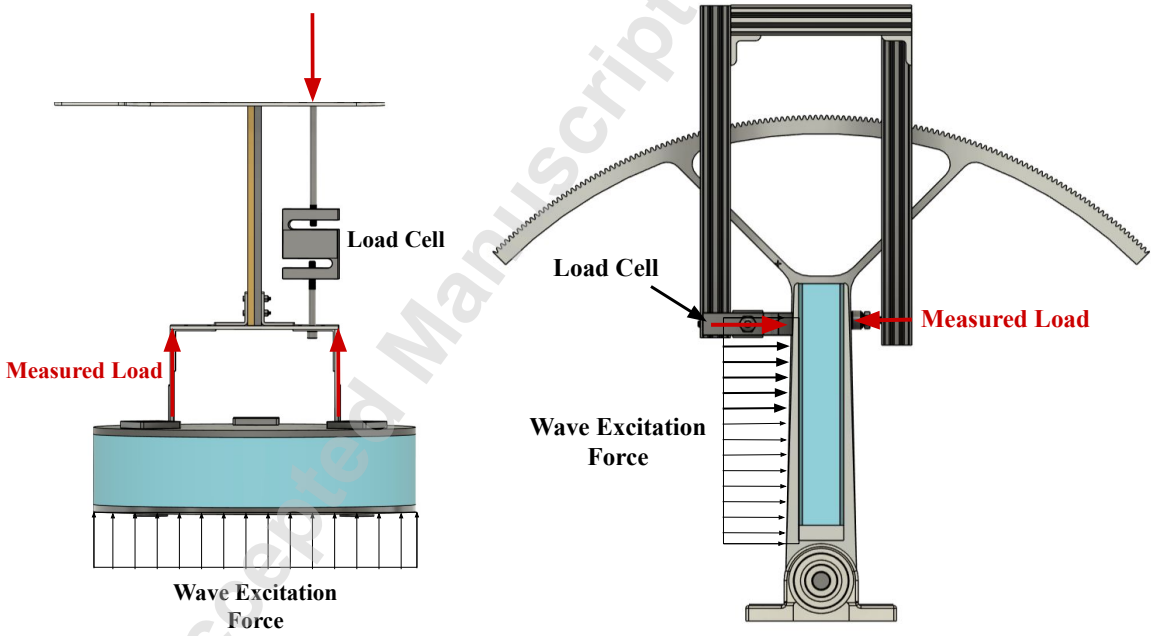

Fig. 12 The point absorber (left) and OSWEC (right) fixed with a load cell linkage. The distributed excitation load from the waves and measured load are depicted. Note that the OSWEC's distributed load is due to the surge force of the wave, which decays exponentially with depth.

defined by the project goals.

Designing an electrical system for small-scale WEC experimentation can become quite complex depending on the project goals. Power distribution, controller power requirements, hardware compatibility, power dissipation or storage, data logging and sensor sensitivities, and software design all must be thoroughly considered to ensure a functioning electrical system. The following subsections detail requirements for each tier, and the design considerations are summarized in Fig. 13. The electrical system designed for this study is shown in Fig. 14, which supports forced oscillation, electrical power production, and electronic controls.

Accepted Manuscript Not Copyedited

Downloaded from http://asmedigitalcollection.asme.org/mechanicaldesign/article-pdf/doi/10.1115/1.4070757/7582635/md-25-1640.pdf by guest on 05 January 2026

Journal of Mechanical Design. Received September 05, 2025;
Accepted manuscript posted January 5, 2026. doi:10.1115/1.4070757
Copyright © 2026 by ASME; reuse license CC-BY 4.0

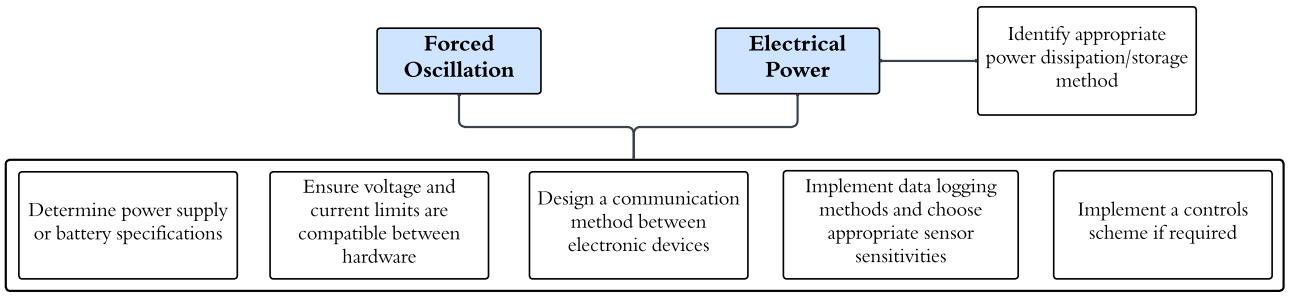

Fig. 13 Electrical design process flowchart.

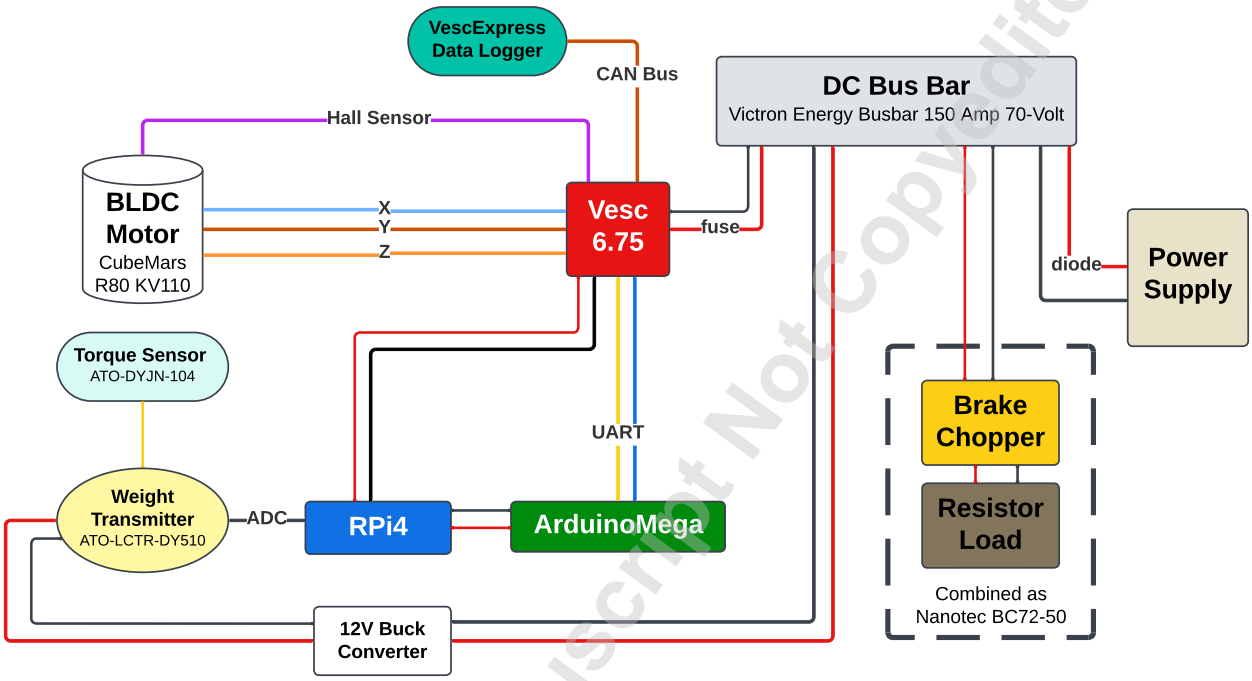

Fig. 14 Full electrical system diagram.

2.3.1 Forced Oscillation. Forced oscillation tests are conducted to determine the radiation force the device imposes. The radiation force ($F_{rad,i}$) can be broken down into the added mass and radiation damping coefficients, derived by Newman [48] as

$$\mathbb{F}_{rad,i} = \omega^2 A_{ij} + i\omega B_{ij}. \tag{20}$$

Experimentally determining the radiation force on the device allows the added mass and damping coefficients to be computed. This is relevant for validating the hydrodynamic coefficients found from an analytical or numerical model. In order to measure this radiation force, the device must be driven at a specified frequency and amplitude without incident waves. This introduced the following requirements:

PTO R11. The mechanical system must be able to be driven at specific frequencies and amplitudes.

FO R1. A variety of input conditions must be programmable and achieve different, desired outputs for each set of conditions.

This was accomplished by utilizing a motor, motor driver (or motor controller), a microcontroller, a power supply, a power distribution method, and a user interface (UI). The motor controller used in this study was a Vesc 6 75. This motor controller works with brushless direct current (BLDC) motors, accommodating the three-phase inputs and hall sensor detection. Vesc also provides a UI called VescTool [56], which allows easy configuration of the motor controller. It also accommodates a data logging tool called VescExpress that stores data in a microSD card. Power was distributed to the components using a DC bus bar, which is effectively a power bar and a ground bar connected to a power supply.

A microcontroller was needed to store code and send commands to the motor controller. The ArduinoMega microcontroller is compatible with the Vesc UART library, which enables reliable, modular communication with the Vesc through well-established protocols. Arduinos are user-friendly and well-documented, so it was chosen for these experiments. The Arduino and the Vesc communicated via UART. To execute different tests based on frequency and amplitude, a RaspberryPi4 (RPi4) with a TFT (touchscreen) was used.

The RPi4 is responsible for displaying the UI, handling serial communication with the Arduino, and transmitting test parameters such as amplitude, frequency, and WEC type. The RPi4 Model B with a 1.5 GHz quad-core ARM Cortex processor and 8 GB of RAM was used. The UI is displayed on a 3.5 inch TFT LCD which attaches to the top of the RPi and has a resolution of 320x240

Author Manuscript Not Copyedited

Downloaded from http://asmedigitalcollection.asme.org/mechanicaldesign/article-pdf/doi/10.1115/1.4070757/7582635/md-25-1640.pdf by guest on 05 January 2026

Journal of Mechanical Design. Received September 05, 2025;
Accepted manuscript posted January 5, 2026. doi:10.1115/1.4070757
Copyright © 2026 by ASME; reuse license CC-BY 4.0

pixels. These components are shown in Appendix B in Fig. 18.

Several key parameters must be configured for the Vesc motor controller, including motor type, battery specifications, and current limits. These parameters are summarized in Table 6 in Appendix B. VescTool also provides real-time plots of motor and system data, used for debugging and monitoring performance.

The Arduino's forced oscillation program took WEC type, desired oscillation frequency, and desired amplitude as inputs. The frequency and amplitude were used to create a sinusoidal current input to the motor, causing the motor to spin back and forth and induce oscillatory motion in the WEC device. A simple gain K_{DC} was used to convert position to current (see Appendix B). For the OSWECs, this gain had a magnitude of 50, corresponding to current amplitudes around 6A. However, the PAs faced much more friction due to their three linear bearings and high gear ratio. For one PA, the gain was 200, corresponding to about 8A. For another PA, the gain was 800, corresponding to around 25A.

The Vesc comes equipped with field oriented control (FOC), allowing tuning of the PI current controller in VescTool. This PI current controller was applied during the forced oscillation tests. Each device required their own K_P and K_I coefficients, as well as individualized observer gains. To find the proper gains, the Ziegler-Nichols method [57] was followed, and the results of this analysis are detailed in Appendix B.

During forced oscillation testing, the Vesc logged motor current data. The torque constant provided by the motor manufacturers was used to translate motor current to motor torque and find the self-imposed radiation force. S-shaped load cells were used to measure the radiation and excitation forces on the fixed devices (see Section 2.2.8, Fig. 12).

Additionally, a static torque sensor was included for torque measurements in the powertrain during forced oscillation testing. The ATO-DY-JN-104 static torque sensor was chosen early on in the project. This sensor was integrated into the motor housing and connected to an ATO-LCTR-DY510 weight transmitter to amplify the measurements. This weight transmitter required a 12V input, so a 12V buck converter was added to the system to accommodate this power requirement. An MCP3008 analog-to-digital converter (ADC) was required to transfer data from the weight transmitter to the RPi4. However, data collection from the torque sensor components was not successful. Using a higher quality sensor and rigorously developing the data acquisition of these components would have improved its contribution.

2.3.2 Electrical Power Production. Once the forced oscillation system was developed, the power production system only introduced these requirements:

Power R1. The motor must apply torque opposing WEC motion to enable power absorption, and the power must be dissipated or absorbed electrically.

Power R2. Capacitive voltage spikes must be mitigated.

The Vesc is equipped to handle regenerative braking (WEC electrical power production). The expected power production from each device was on the order of 100 mW. Handling this power production can be accomplished using a rechargeable battery, regenerative power supply, or dissipative load. This design used a standard non-regenerative power supply with a dissipative load. Due to initial expectations of larger power, the dissipative load took the form of a brake chopper with an internal resistor load.

The Nanotec BC72-50 brake chopper with a 4.7 Ohm resistor was chosen and handled voltage levels up to 48V. The brake chopper engaged the resistor when the bus voltage exceeded a pre-programmed threshold. Typically, this threshold is set to just above the bus voltage, so the resistor engages when there is net power generation on the bus. This safeguards a standard power supply while avoiding unnecessary resistive loss. However, time-varying resistor engagement introduces additional nonlinear dynamics that would create complexities in the hydrodynamic model that were out of scope. In this system, the chopper voltage threshold (12V) was set below the bus voltage (48V), introducing the equivalent dynamics of a resistor in parallel with the bus.

Upon experimentation, the other electrical components would not turn on when the brake chopper was connected to the bus. Therefore, the chopper was ultimately removed, leaving only the internal series parasitic resistance to absorb the load. This was sufficient for power generation on the order of mW, but for larger systems, it is recommended to replace the power supply and brake chopper with a rechargeable battery. However, this was not a priority for small-scale bench-top prototyping, as power production was small compared to parasitic resistance in the system. The final configuration used during experimentation did not include the torque sensor or the brake chopper, and is shown in Appendix B.

To implement electronic controls for power production, the following requirement was introduced: *Control R1. The motor must receive current control commands, and the motor controller must obtain current and angular position feedback from the motor with a specified resolution.* The implemented controls code created desired current inputs based on optimal control theory for reactive control [52]. The PTO damping (B_{PTO}) and stiffness (K_{PTO}) are defined as

$$B_{PTO} = B_{ij} \tag{21}$$

and

$$K_{PTO} = \omega^2 \left(M_{ij} + A_{ij}\right) - K. \tag{22}$$

B_{ij} and A_{ij} were calculated for each operating frequency beforehand in Capytaine. Using these coefficients, a standard PI control scheme was implemented between WEC speed and desired force. A control diagram for both forced oscillation and power production is shown in Appendix B.

To handle capacitive voltage spikes upon turning on the system, initial designs included a precharge relay and resistor, but these were found to be unnecessary due to the system's substantial parasitic resistance.

The custom electrical system was the most challenging part of this design. It is common practice to use a fully integrated sensing, motor control, state machine, logging, and user interface system rather than a custom system integrating many components. However, the electronics design for small-scale WEC prototyping is continuously evolving, and the recommended methodology for custom electronics design is thoroughly detailed.

3 Generalized Requirements

Requirements were detailed for each individual analysis throughout the report. However, several of these requirements were specific to the presented WEC prototypes. To ensure this work remains generalizable for other WEC developers, universal requirements are presented in Table 4. It is structured such that high-level requirements (in bold text) are listed and deconstructed into their sub-requirements. These requirements are applicable to all small-scale WEC design endeavors. Requirements in the **A** category, referring to the test facility and fluid regime, must be considered first in the design process. **B** category requirements (related to device resonance) must be considered next, and, if a PTO is included, **D** requirements should be considered concurrently. Next, the **C** category (mooring) requirements should be incorporated into the design process. The remainder of the requirements are contingent upon the experimental goals and should be incorporated concurrently, if relevant. A summary of this guidance is provided in Table 5.

4 Discussion

The presented design methodology and resulting prototypes coalesce years of design iterations and trial and error. The key analyses for small-scale WEC prototype design are compiled and organized

Accepted Manuscript Not Copyedited

Downloaded from http://asmedigitalcollection.asme.org/mechanicaldesign/article-pdf/doi/10.1115/1.4070757/7582635/md-25-1640.pdf by guest on 05 January 2026

Journal of Mechanical Design. Received September 05, 2025;
Accepted manuscript posted January 5, 2026. doi:10.1115/1.4070757
Copyright © 2026 by ASME; reuse license CC-BY 4.0

Table 4 Generalized requirements for small-scale WEC prototyping.

Requirement	Description	Priority	In Text Ref.
A	**The dominant physical processes represented in the prototype and testing facility must match the dominant physical processes represented by the model.**	1	Fluid R1&2
A.1	The chosen test facility must be capable of producing the desired fluid regime.	1	
A.2	The chosen scaling method must coincide with physical assumptions of the fluid regime.	1	
A.3	The analytical, numerical, or computational model must be capable of representing the desired fluid regime.	1	
B	**The prototype must be designed to resonate with the incident waves.**	2	
B.1	The natural frequency of oscillation of the device must meet or approach the wave frequency range of the fluid regime and testing facility.	2	Geom R2
B.2	If the devices will not resonate with the incident waves from their pure hydrodynamic properties, the implemented PTO must be capable of tuning the device's natural frequency.	3	Control R1
C	**The prototype must include a mooring structure that is compatible with the testing facility and the experimental goals.**	1	
C.1	The mooring structure must avoid shedding vortices (which can cause vortex induced vibrations) or other nonlinear effects that are not accounted for by the model.	1	Moor R4
C.2	The mooring structure must achieve the device draft.	1	Moor R5
D	**If a PTO is included, it must be capable of producing mechanical power.**	1	
D.1	The friction in the PTO must be minimized.	1	PTO R1
D.2	The force or torque applied by the device due to wave excitation must be able to overcome the friction or pressure in the PTO.	1	PTO R2&3
E	**If forced oscillation tests are required by the project goals, an electronics system must be integrated and able to drive the prototype.**	2	PTO R11
E.1	A variety of input conditions must be programmable and achieve distinct, desired outputs for each set of conditions.	2	FO R1
E.2	All hardware must be rated with voltage and current limits that are compatible with each other and the expected power requirement to drive the device.	1	Elec R1
E.3	A data logging method must be included, and each sensor should be selected with appropriate resolution for the project goals and device scale.	1	Elec R2
F	**If electrical power production is included in the project goals, an electronics system must be integrated and include a method to handle power production.**	2	Power R1
F.1	All hardware must be rated to handle the electrical power produced by the device OR have a protection mechanism in place.	1	Elec R1
F.2	See Requirement E.3	1	
G	**If electronic controls are required by the project goals, an electrical system must be integrated and capable of controlling the device motion.**	2	
G.1	Communication between electronic devices must be sophisticated enough to implement a controller.	2	Control R1
G.2	See Requirement F.1	1	
G.3	See Requirement E.3	1	

Table 5 Guidance on when to incorporate requirements into the design process.

Requirement Group	Design Process
A	Overarching, Step 1
B, **D**	Mechanical, Step 2
C	Mechanical, Step 3
E, **F**, **G**	Electrical, Step 4

into overarching, mechanical, and electrical. We emphasize the critical design considerations to address early in the design process and frequently revisit as the project evolves. Consolidating the design process as such will streamline future small-scale WEC prototype development, contributing to the production of high-quality, fundamental WEC research.

Numerical simulations were useful for gaining intuition of the WEC hydrodynamic behavior and informing design decisions. However, BEM simulations neglect nonlinear and viscous forces, which can result in large errors in device motion estimations (up to 35% error in natural period for the OSWEC). If possible, small-scale WECs prototypes should be hydrodynamically tested or modeled in higher fidelity software early in the design process, assessing deviations from the model before finalizing designs. It is possible BEM's shortcomings are exacerbated at the small-scale. This is an ongoing area of follow-on research.

Accepted Manuscript Not Copyedited

Downloaded from http://asmedigitalcollection.asme.org/mechanicaldesign/article-pdf/doi/10.1115/1.4070757/7582635/md-25-1640.pdf by guest on 05 January 2026

Journal of Mechanical Design. Received September 05, 2025;
Accepted manuscript posted January 5, 2026. doi:10.1115/1.4070757
Copyright © 2026 by ASME; reuse license CC-BY 4.0

Several other PTO schemes were investigated prior to the rack and pinion designs. The PA originally featured a leadscrew PTO system, but the static friction in this powertrain was prohibitive at the small-scale. Eventually, a rack and pinion PTO was designed to satisfy the PA requirements. Maintaining rack alignment and gear meshing was relatively simple. The rack and pinion's ability to overcome friction was superior to other investigated PTO systems, though a smaller gear ratio would have improved performance.

The OSWEC's first PTO was a belt-driven gear box, equipped with four gears, and attempted to optimize the final gear ratio. However, the friction was so prohibitive that the gears would not rotate even when actuated by hand. The next design involved a string-spring pulley system. This worked well for minimizing friction; however, the likelihood of the string going slack during experimentation was significant. Additionally, controlling the OSWECs requires positive stiffness inputs, increasing the risk of losing string tension. Finally, a curved rack was designed. This introduced challenges in maintaining hydrostatic stability, but allowed the most control over the device and greatly reduced the friction in the powertrain. The rack and pinion PTOs were the best option for the small-scale WEC prototypes, as they had the least friction, the ability to be driven, and were straightforward to implement.

If these systems were to be re-built, the three shafts and linear bearings would be eliminated from the PA design. The shafts over-constrained the system, requiring high precision during manufacturing. Aligning the shafts was challenging and not always effective, as was leveling the PA float marine foam to the desired precision. To mitigate these misalignment effects, self-aligning bearings were used, improving the device motion compared to the original linear sleeve bearing and producing smooth motion during dry tests. However, once water entered the bearings, viscous friction was introduced and constrained the float motion. Additionally, the surge force from the incident waves introduced large normal forces in the bearings, further increasing the bearing friction force. To mitigate this, the PAs needed to move slightly in other degrees of freedom (primarily pitch) to improve the heave motion of the device. This is an important conclusion for small-scale PA design, in that these devices should be designed with the intention of being excited in additional degrees of freedom.

Depending on the experimental goals, a custom electrical system may be useful to achieve specialized results or data collection. However, the electrical system requirements could have been more easily satisfied using already integrated technology, such as Speedgoat [58]. Vesc motor controllers are not designed for scientific inquiry, and their sensor precision is not documented or available. However, the data logging capabilities of the VescExpress were convenient and satisfied the requirements. The RPi4, TFT, and ArduinoMega combination could specify the desired test conditions and execute the expected commands. Understanding the expected power production of the system is crucial for sizing the electrical system. The system in this report was over-sized, and resulted in sub-optimal operation. A different motor, motor controller, and torque sensor are recommended for small-scale prototyping.

5 Conclusions

In this work, a concrete methodology and requirements for designing small-scale WEC prototypes was presented. Relevant prototyping considerations are detailed and recommendations are made regarding design process flow. This methodology was informed by a years-long WEC prototyping project and applies to multiple WEC architectures. These architectures were experimentally tested and the design process validated. Alternative design methods and previous design iterations are briefly discussed. All CAD drawings, analysis scripts, and embedded code used in these designs can be found at the SEA Lab WEC Prototyping Github. The bill of materials for each subsystem are detailed in Appendix C.

6 Acknowledgments

This project was funded by the Cornell Atkinson Center for Sustainability Summer Mentored Research Grant 2023 and the FAST Grant 2024, the Sea Grant Regional Research Project No.: R/ATD-18-NESG, the United States Department of Energy Testing and Expertise in Marine Energy (TEAMER) RFTS 12, and the National Science Foundation (NSF) Graduate Research Fellowship under Grant DGE–2139899.

Thank you to the many students who assisted on this project over several years, notably Benjamin Choe, Nathaniel DeGeode, Madison Dietrich, Mahika Goel, Sabian Grier, Robert Iverson, Miriam Levesque, Larry Lu, Haley Merchant, Andrea Miramontes Serrano, Kavya Mittha, Nelson Ooi, Cecily Pokigo, Nathan Rahklin, Kelvin Resch, and Vidhi Srivastrava.

Nomenclature

L = wavelength [m]
V = fluid velocity [m/s]
g = gravitational constant [m/s^2]
B = damping coefficient [kg/s]
$\mathbb{X}$ = complex body motion [m or deg]
I = mass moment of inertia [kg or kg-m^2]
A = added mass [kg or kg-m^2]
K = hydrodynamic stiffness [kg-m^2/s^2]
m = mass [kg]
h = height [m]
l = length [m]
t = thickness [m]
r = radius [m]
A_{wp} = water plane area [m^2]
T_n = natural period [s]
T = torque [N-m]
V_{sub} = submerged volume [m^3]
c_b = center of buoyancy [m]
c_g = center of gravity [m]
t = time [s]
Ω = motor angular velocity [rpm]
C = load capacity [lbf or N]
P = applied load [lbf or N]
L = lifetime [millions of revolutions]
σ_t = Lewis bending stress [psi or Pa]
P_d = diametral pitch
F = face width [m]
k_b = torque constant [N-m/A]
W_t = tangential load [lbf or N]
p = Hertzian contact pressure [psi or Pa]
E = modulus of elasticity [psi or Pa]
P = power [W]

Greek Letters

ρ = fluid density [kg/m^3]
γ = viscous damping term [kg/s]
ω = frequency [rad/s]
ϕ = rotation angle [deg]

Dimensionless Groups

Fr = Froude Number
RAO = response amplitude operator
λ = ratio of wavelengths for Froude scaling
γ_{nl} = nonlinear drag term
γ_i = phase angle [rad]
GR = gear ratio
Y = Lewis form factor
ν = Poisson's ratio

Accepted Manuscript Not Copyedited

Downloaded from http://asmedigitalcollection.asme.org/mechanicaldesign/article-pdf/doi/10.1115/1.4070757/7582635/md-25-1640.pdf by guest on 05 January 2026

Journal of Mechanical Design. Received September 05, 2025;
Accepted manuscript posted January 5, 2026. doi:10.1115/1.4070757
Copyright © 2026 by ASME; reuse license CC-BY 4.0

Superscripts and Subscripts

i, j = degree of freedom
p = prototype
f = full-scale
w = water
3 *or* 33 = heave degree of freedom
5 *or* 55 = pitch degree of freedom
e = excitation
rad = radiation
g = due to gravity
b = buoyancy
v = viscous
n = natural
gen = generator
d = dynamics
eff = effective
$mech$ = mechanical
opt = optimal

References

[1] Parkinson, S. C., Dragoon, K., Reikard, G., García-Medina, G., Özkan Haller, H. T., and Brekken, T. K., 2015, "Integrating ocean wave energy at large-scales: A study of the US Pacific Northwest," Renewable Energy, **76**, pp. 551–559.

[2] Sasaki, W., 2017, "Predictability of global offshore wind and wave power," International Journal of Marine Energy, **17**, pp. 98–109.

[3] Hagerman, G., Scott, G., and Jacobson, P. T., 2011, "Mapping and Assessment of the United States Ocean Wave Energy Resource," Electric Power Research Inst. (EPRI), Palo Alto, CA (United States), doi: 10.2172/1060943.

[4] Katinas, V., Gecevicius, G., and Marciukaitis, M., 2018, "An investigation of wind power density distribution at location with low and high wind speeds using statistical model," Applied Energy, **218**, pp. 442–451.

[5] Levi Kilcher, M. L., Michelle Fogarty, 2021, "Marine Energy in the United States: An Overview of Opportunities," National Renewable Energy Laboratory.

[6] of Energy, U. D., 2015, "Quadrennial Technology Review 2015," https://www.energy.gov/quadrennial-technology-review-2015

[7] Watson, D., 2016, "Pelamis Wave Power P2 Demonstration at EMEC," https://tethys.pnnl.gov/project-sites/pelamis-wave-power-p2-demonstration-emec

[8] 2023, "CorPower Ocean deploys C4 Wave Energy Converter." https://corpowerocean.com/corpower-oceans-wave-energy-converter-deployed/

[9] Office, W. P. T., 2024, "Wave Energy Converter Completes Deployment Despite Hurricane-Fueled Waves," https://www.energy.gov/eere/water/articles/wave-energy-converter-completes-deployment-despite-hurricane-fueled-waves

[10] Sanderson, C., 2024, "'World first' wave energy converter deployed at US Navy test site in Hawaii," https://www.rechargenews.com/energy-transition/-world-first-wave-energy-converter-deployed-at-us-navy-test-site-in-hawaii/2-1-1683629

[11] Bingyong Guo, J. V. R., 2021, "A review of wave energy technology from a research and commercial perspective," IET Renewable Power Generation.

[12] Dalton, G., Alcorn, R., and Lewis, T., 2010, "Case study feasibility analysis of the Pelamis wave energy convertor in Ireland, Portugal and North America," Renewable Energy, **35**(2), pp. 443–455.

[13] Francis Karagjozi, G. P., 2016, "Enabling factors to make Ocean Wave Power a competitive renewable energy source," Master's thesis, Swedish University of Agricultural Sciences.

[14] Fard, H., Mahmoodi, K., and Vaghefi, M., 2025, "Geometry optimization of a two-body heaving point absorber wave energy converter based on the long-term Oman Gulf wave climate," Renewable Energy, **253**, p. 123498.

[15] Mi, J., Huang, J., Li, X., Ahmed, A., Yang, L., Chung, U., Datla, R., Hajj, M., and Zuo, L., 2024, "Oscillating surge wave energy converter using a novel above-water power takeoff with belt-arc speed amplification," Ocean Engineering, **310**(Part 1), p. 118503.

[16] Liu, K., Chen, D., Liang, P., Yao, X., Deng, Z., Xu, K., Xin, Y., and Huang, D., 2025, "SPH modeling and experimental validation on power performance and dynamic response of a novel swing-wing wave energy converter," Energy Conversion and Management, **325**, p. 119420.

[17] Gayathri, R., Chang, J.-Y., Tsai, C.-C., and Hsu, T.-W., 2024, "Wave Energy Conversion through Oscillating Water Columns: A Review," Journal of Marine Science and Engineering, **12**(2).

[18] Cao, D., He, J., and Chen, H., 2024, "Empirical Predictions on Wave Overtopping for Overtopping Wave Energy Converters: A Systematic Review," Processes, **12**(9).

[19] Ghribi, D., Bruyère, J., Velex, P., Octrue, M., and Haddar, M., 2012, "A Contribution to the Design of Robust Profile Modifications in Spur and Helical Gears by Combining Analytical Results and Numerical Simulations," Journal of Mechanical Design, **134**(6), p. 061011.

[20] Demeulenaere, B., Verschuure, M., Swevers, J., and De Schutter, J., 2009, "A General and Numerically Efficient Framework to Design Sector-Type and Cylindrical Counterweights for Balancing of Planar Linkages," Journal of Mechanical Design, **132**(1), p. 011002.

[21] Wang, Z., Melkote, S., and Rosen, D. W., 2023, "Generative Design by Embedding Topology Optimization into Conditional Generative Adversarial Network," Journal of Mechanical Design, **145**(11), p. 111702.

[22] Shadman, M., Estefen, S. F., Rodriguez, C. A., and Nogueira, I. C., 2018, "A geometrical optimization method applied to a heaving point absorber wave energy converter," Renewable Energy, **115**, pp. 533–546.

[23] Zeinali, S., Wiktorsson, M., Forsberg, J., Lindgren, G., and Lindström, J., 2024, "Optimizing the hydraulic power take-off system in a wave energy converter," Ocean Engineering, **310**, p. 118636.

[24] Sergiienko, N., Cazzolato, B., Ding, B., and Arjomandi, M., 2016, "An optimal arrangement of mooring lines for the three-tether submerged point-absorbing wave energy converter," Renewable Energy, **93**, pp. 27–37.

[25] Agrawal, S. K., Kumar, S., and Yim, M., 2002, "Polyhedral Single Degree-of-freedom Expanding Structures: Design and Prototypes," Journal of Mechanical Design, **124**(3), pp. 473–478.

[26] Tang, R., Meng, Q., Xie, F., Liu, X.-J., and Wang, J., 2023, "Structural Designs of Novel Deployable Polyhedral Grippers for Noncontact Capturing Missions," Journal of Mechanical Design, **146**(4), p. 043302.

[27] Juan, J., Núria Salán, M., Silva, A., and Tornero, J. A., 2019, "Design of a Prototype for the In Situ Forming of a Liquid-Infused Preform Process," Journal of Mechanical Design, **142**(1), p. 015001.

[28] Briot, S., Arakelian, V., and Guégan, S., 2008, "Design and Prototyping of a Partially Decoupled 4-DOF 3T1R Parallel Manipulator With High-Load Carrying Capacity," Journal of Mechanical Design, **130**(12), p. 122303.

[29] Lauff, C. A., Kotys-Schwartz, D., and Rentschler, M. E., 2018, "What is a Prototype? What are the Roles of Prototypes in Companies?" Journal of Mechanical Design, **140**(6), p. 061102.

[30] Joensen, B. and Bingham, H. B., 2024, "Economic feasibility study for wave energy conversion device deployment in Faroese waters," Energy, **295**, p. 130869.

[31] Kofoed, J. P., Frigaard, P., Friis-Madsen, E., and Sørensen, H. C., 2006, "Prototype testing of the wave energy converter wave dragon," Renewable Energy, **31**(2), pp. 181–189, Marine Energy.

[32] Hansen, C. A. and Özkil, A. G., 2020, "From Idea to Production: A Retrospective and Longitudinal Case Study of Prototypes and Prototyping Strategies," Journal of Mechanical Design, **142**(3), p. 031115.

[33] Starkey, E. M., Menold, J., and Miller, S. R., 2019, "When Are Designers Willing to Take Risks? How Concept Creativity and Prototype Fidelity Influence Perceived Risk," Journal of Mechanical Design, **141**(3), p. 031104.

[34] Rodríguez-Calero, I., Daly, S. R., Burleson, G., and Sienko, K. H., 2023, "Prototyping Strategies to Engage Stakeholders During Early Stages of Design: A Study Across Three Design Domains," Journal of Mechanical Design, **145**(4), p. 041413.

[35] Menold, J., Jablokow, K., and Simpson, T., 2017, "Prototype for X (PFX): A holistic framework for structuring prototyping methods to support engineering design," Design Studies, **50**, pp. 70–112.

[36] Camburn, B. and Wood, K., 2018, "Principles of maker and DIY fabrication: Enabling design prototypes at low cost," Design Studies, **58**, pp. 63–88.

[37] Lauff, C., Menold, J., and Wood, K. L., 2019, "Prototyping Canvas: Design Tool for Planning Purposeful Prototypes," Proceedings of the Design Society: International Conference on Engineering Design, **1**(1), p. 1563–1572.

[38] Vitale, O., Ahmed, A., and Haji, M., 2025, "TEAMER," Marine and Hydrokinetic Data Repository, Cornell University, https://mhkdr.openei.org/submissions/637, https://mhkdr.openei.org/submissions/637

[39] Lomonaco, P., 2024, Private Communication.

[40] P. D. McCormack, L. C., 1973, *Physical Fluid Dynamics*, Academic Press Inc.

[41] Martić, I., Degiuli, N., and Grlj, C. G., 2024, "Scaling of wave energy converters for optimum performance in the Adriatic Sea," Energy, **294**, p. 130922.

[42] Windt, C., Davidson, J., and Ringwood, J. V., 2021, "Numerical analysis of the hydrodynamic scaling effects for the Wavestar wave energy converter," Journal of Fluids and Structures, **105**, p. 103328.

[43] Bhinder, M. A., Babarit, A., Gentaz, L., and Ferrant, P., 2015, "Potential time domain model with viscous correction and CFD analysis of a generic surging floating wave energy converter," International Journal of Marine Energy, **10**, pp. 70–96.

[44] 2018, "An improved boundary element method for modelling a self-reacting point absorber wave energy converter," Acta Mechanica Sinica.

[45] Majid Bhinder, L. G. P. F., Aurélien Babarit, 2012. ffhal-01202082, "Effect of viscous forces on the performance of a surging wave energy converter," *22nd International Conference on Ocean, Offshore and Artic Engineering (ISOPE2012), Rhodes, Greece*.

[46] Ancellin, M. and Dias, F., 2019, "Capytaine: a Python-based linear potential flow solver," Journal of Open Source Software, **4**(36), p. 1341.

[47] Kurnia, R. and Ducrozet, G., 2023, "NEMOH: Open-source boundary element solver for computation of first- and second-order hydrodynamic loads in the frequency domain," Computer Physics Communications, **292**, p. 108885.

[48] Newman, J., 2017, *Marine Hydrodynamics*, The MIT Press, Cambridge, Massachusetts, 40th Anniversary Edition.

[49] Nathan Tom, Y.-H. Y., Michael Lawson and Wright, A., 2015, "Preliminary Analysis of an Oscillating Surge Wave Energy Converter with Controlled Geometry," National Renewable Energy Laboratory.

[50] Alaa Ahmed, J. H. A. S. R. D. L. Z. M. H., Lisheng Yang, 2024, "Performance characterization and modeling of an oscillating surge wave energy converter," Nonlinear Dynamics.

[51] Olivia Vitale, R. M. P. L. M. H., Alaa Ahmed, in prep, "HetWECs: an experimental investigation of heterogeneous wave energy converter arrays," Renewable Energy.

Downloaded from http://asmedigitalcollection.asme.org/mechanicaldesign/article-pdf/doi/10.1115/1.4070757/7582635/md-25-1640.pdf by guest on 05 January 2026

Journal of Mechanical Design. Received September 05, 2025;
Accepted manuscript posted January 5, 2026. doi:10.1115/1.4070757
Copyright © 2026 by ASME; reuse license CC-BY 4.0

[52] Falnes, J. and Kurniawan, A., 2020, *Ocean Waves and Oscillating Systems*, Cambridge University Press, Cambridge, United Kingdom, Second Edition.
[53] Lewis, E. V., 1989, *Principles of Naval Architecture. vol 1; Stability and Strength ... vol 3; motions in waves and controllability*, Society of Naval Architects and Marine Engineers.
[54] Ahmed, A., 2024, Private Communication.
[55] Xu, F., Ding, N., Li, N., Liu, L., Hou, N., Xu, N., Guo, W., Tian, L., Xu, H., Lawrence Wu, C.-M., Wu, X., and Chen, X., 2023, "A review of bearing failure Modes, mechanisms and causes," Engineering Failure Analysis, **152**, p. 107518.
[56] Vedder, B., "Vesc Tool," https://vesc-project.com/vesc_tool
[57] Ziegler, J. G. and Nichols, N. B., 2022, "Optimum Settings for Automatic Controllers," Transactions of the American Society of Mechanical Engineers, **64**(8), pp. 759–765.
[58] "Speedgoat," https://www.speedgoat.com/
[59] Richard G. Budynas, J. K. N., 2015, *Shigley's Mechincal Engineering Design, Tenth Edition*, McGraw-Hill Education, 2 Penn Plaza, New York, NY 10121.
[60] Hertz, H., 1896, "Miscellaneous papers," London: Macmillan, New York, Macmillan and co.

Appendix A: Supplemental Mechanical Design

This appendix details additional analyses and designs for the mechanical systems detailed in this study.

Alternative Gear Ratio Determination. The motor's maximum allowable torque and RPMs are 4 N-m and 3000 RPMs, respectively. These were our main restrictions when choosing a gear ratio and needed to be satisfied for both PTO powered tests and forced oscillation testing. For the forced oscillation tests, the motor torque T_{motor} was computed as

$$T_{motor} = T_{m,amp} \sin(\omega t) \tag{A1}$$

where the subscript m, amp denotes the amplitude of the torque programmed to the motor. This was programmed and measured as current, and can be converted the torque using the torque constant available from the manufacturer. For the PTO powered tests, motor torque was calculated as

$$T_{motor} = I_{motor}\ddot{\phi} \cdot GR - T_{gen} + T_{friction} \tag{A2}$$

where GR is the gear ratio, gen denotes torque due to the generator implementing reactive controls, and $T_{friction}$ indicates friction within the drivetrain itself. This was split into static friction, which was only active at zero-velocity moments, and dynamic friction

$$T_{dynamic} = T_d sgn(\dot{\phi}) + b \cdot GR \cdot \dot{\phi} \tag{A3}$$

where T_d is the dynamic friction magnitude, $sgn(\dot{\phi})$ accounts for the bi-directionality of the motor, and b is the viscous friction coefficient. The inertia in the motor, I_{motor}, was calculated as

$$I_{motor} = \frac{1}{2} m_{motor} r_{motor}^2 \tag{A4}$$

where m is the rotating mass and r is the rotation radius. The motor's angular velocity (Ω_{motor}) was calculated using

$$\Omega_{motor} = \frac{60}{2\pi} GR \cdot \dot{\phi} \tag{A5}$$

Different gear ratios were swept over a range of frequencies and amplitudes to determine our bounds for acceptable gear ratios. However, the friction values were challenging to quantify before the electrical system was functional. We estimated measurements using dynamometers, but they were not precise. Without accurate powertrain friction values, our model predicted that any gear ratio would be acceptable. It was not until the devices and motor housings were completely constructed that we were able to choose proper pinions for the PTO. We initially chose the smallest pinions possible in hopes to produce fast motor motion with low torque. However, at such a large gear ratio, the devices could not overcome the static friction in the powertrain and barely moved in our preliminary tests. We nearly doubled the size of our pinions for our devices to be able to spin the motor.

This model would be more effective with accurate friction estimations. Estimating the friction in the powertrain is especially relevant at such a small scale, where even small amounts of friction are extremely challenging for the device to overcome.

Bearing Load Calculations. We needed to determine the required load capacity (C) [59], of the bearings, defined as

$$C = P\left(\frac{L}{10^6}\right)^{1/k} \tag{A6}$$

where L is lifetime in millions of revolutions, P is the applied load, and k is a factor ranging from 3-3.3. To determine the lifetime, the total number of expected cycles per device was computed. Each device must be able to withstand 144 trials in the basin. Each trial lasts for 180 s, and the fastest wave period the device will experience is 1 s. This brings the total required lifetime of each bearing 25,920 cycles.

To find the applied load, wave force data from full-scale BEM simulations was computed and scaled down for the tank experiments. The maximum wave load the PA will experience corresponds with the largest wave amplitude, which is 0.10 m at the tank scale. The maximum applied load was determined to be 42.56 N, or about 10 lbf. Plugging these values into Eq. A6, the required load capacity of the bearings was 0.126 N or 0.028 lbf. However, we expected a much higher required load capacity and used flange-mount linear sleeve bearings with a capacity of 300 lbf (1330 N).

Gear Teeth Loading Calculations. The Lewis bending stress (σ_t) [59] is defined as

$$\sigma_t = \frac{W_t P_d}{FY} \tag{A7}$$

where W_t is the tangential load, P_d is the diametral pitch, F is the face width, and Y is the Lewis form factor. The maximum tangential load applied is 1.92 lbf (8.54 N) for the PA's pinion and 1.55 lbf (6.9 N) for the OSWEC's. Imperial units are used for ease of calculation. The PAs have a diametral pitch of 0.039 in^{-1} (0.0015 m^{-1}) with a face width of 0.236 in (6 mm) and a form factor estimated at 0.4. This yields a maximum bending stress of 0.801 psi (5.5 kPa). The PA rack and pinion are made of brass, which has a yield stress of of 20 ksi (138 MPa), so this bending stress is not concerning. The OSWEC pinion has a diametral pitch of 0.059 in^{-1} (0.0023 m^{-1}), a face width of 0.59 in (15 mm), and a form factor of 0.3, yielding a maximum bending stress of 0.517 psi (3.6 kPa). The OSWEC pinion is made of 316 stainless steel, with a Young's modulus of 29 msi (96.5 MPa).

The bending stress on the gears is negligible given the loads we apply and the material of the gears. However, the contact pressure was potentially a larger risk factor for the gears. The Hertzian contact pressure (p) [60] is defined as

$$p = \sqrt{\frac{E^* W}{\pi F}\left(\frac{1}{r_{eg}} + \frac{1}{r_{ep}}\right)} \tag{A8}$$

where $W = W_t/\cos\phi$ where ϕ is the pressure angle, r_{eg} and r_{ep} are the equivalent radii of the cylinders ($r_{pitch} \cdot \sin\phi$), and E^* is the effective modulus of elasticity, defined as

$$E^* = \frac{E}{(1-\nu^2)} \tag{A9}$$

when the contact materials are the same. When they are made of two different materials, it is defined as

$$\frac{2}{E^*} = \frac{(1-\nu_1^2)}{E_1} + \frac{(1-\nu_2^2)}{E_2} \tag{A10}$$

Accepted Manuscript Not Copyedited

Downloaded from http://asmedigitalcollection.asme.org/mechanicaldesign/article-pdf/doi/10.1115/1.4070757/7582635/md-25-1640.pdf by guest on 05 January 2026

Journal of Mechanical Design. Received September 05, 2025;
Accepted manuscript posted January 5, 2026. doi:10.1115/1.4070757
Copyright © 2026 by ASME; reuse license CC-BY 4.0

For the PA, this yielded a maximum contact pressure of 7992 psi (55 MPa), and for the OSWEC, only 153.7 psi (1.06 MPa). Based on this analysis, our gears would confidently withstand the loads we applied.

From these values, the factor of safety for each failure mode can be determined using

$$N = \frac{S_y}{\sigma} \tag{A11}$$

Alternative Device Fixture. This fixture used a custom-machined component to fix the d-profile shaft in the motor subassembly in place. This would introduce a load on the static torque sensor integrated into the motor subassembly, allowing wave excitation force measurements to be extrapolated. The design is shown in Fig. 15.

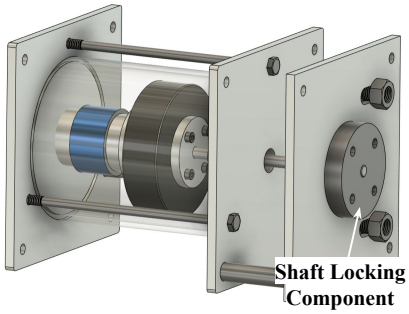

Fig. 15 Component to lock motor shaft and subsequently fix the devices.

Appendix B: Supplemental Electrical Material

Control Diagram. The control diagram for both forced oscillation and power production is shown in Fig. 16.

Electronics Design Used in Experiments. Figure 17 shows the final electrical system design that was actually used during experimentation. The break chopper, static torque sensor, weight transmitter, and buck converter were removed during experiments.

RPi Hardware. Photos of the RPi4 and TFT screen hardware are shown in Fig. 18.

Vesc Parameters. The parameters programmed into the Vesc motor controller are shown in Table 6. To find the proper gains, the Ziegler-Nichols method [57] was followed, setting K_I equal to zero and incrementally increasing K_P until smooth motion was observed. The K_P value at this point is called K_u. Then, K_P was set equal to $0.45K_u$ and K_I equal to $0.54K_u/T_u$ where T_u is the oscillation period. However, each device deviated from these values. Further trial and error was necessary to finalize these parameters, shown in Table 7.

Table 6 VESC configuration parameters.

Setting Name	Value
Motor	Mini outrunner (approx. 75 g)
Battery Type	`BATTERY_TYPE_LIION_3_0_4_2`
Battery Cell Series	4
Battery Capacity	6.000 Ah
Battery Current Regen	-30 A
Motor Max Current	13 A
Battery Voltage Cutoff Start	13 V
Battery Voltage Cutoff End	12 V

Table 7 FOC parameters tuned using VescTool current controller.

Device Type and Number	K_P	K_I	Observer Gain
OSWEC 1	0.0525	100	500
OSWEC 2	0.0525	100	500
PA 3	1.0	101	0.0
PA 4	0.009	1.0	1.0

Appendix C: Required Materials, Machining, and Cost

The machines required are as follows:

(1) Waterjet - precision machining of aluminum and steel
(2) CNC - precision machining of aluminum and steel
(3) Laser cutter - machining of acrylic
(4) Drill press/mill - precision machining of through holes and counter-bores
(5) Lathe - machining of motor-to-shaft attachment
(6) 3D printer - production of shaft housings

The bill of materials for the point absorber, oscillating surge, motor housing, and electronics are found in Tables 8 through 11.

Accepted Manuscript Not Copyedited

Downloaded from http://asmedigitalcollection.asme.org/mechanicaldesign/article-pdf/doi/10.1115/1.4070757/7582635/md-25-1640.pdf by guest on 05 January 2026

Journal of Mechanical Design. Received September 05, 2025;
Accepted manuscript posted January 5, 2026. doi:10.1115/1.4070757
Copyright © 2026 by ASME; reuse license CC-BY 4.0

Table 8 Point absorber bill of materials. All part numbers correspond with McMaster-Carr parts.

Component/System	Part Description	Part #	Unit Cost
PTO			
Rack	Metal Gear Rack - 20 Degree Pressure Angle, 1 Module, 300 mm Long, 9 mm Pitch Height, brass	2485N237	$36.15
Pinion	Metal Gear - 20 Degree Pressure Angle Round with Set Screw, 1 Module, 50 Teeth, 6 mm Face Width	2664N503	$45.41
Track roller for rack	Maintenance-Free Threaded Track Roller, Steel Flat Roller, 1" Diameter x 5/8" Wide Roller	6721K5	$33.65
Float bearings + housing	Chemical-Resistant Flange-Mount Linear Sleeve Bearing 0.0015" Shaft Clearance, 3-3/8" x 1-5/8" x 1-5/8" Overall	64825K212	$228.16
Support rods	Tapped Linear Motion Shaft, Tapped on Both Ends, 440C Stainless Steel, 1/2" Diameter, 18" Long	1240K143	$103.14
Rack ground brackets	Galvanized Steel Corner Bracket, 1.5" x 1.5" x 1.25"	17715A75	$1.67
Support rod housing	Support rod end caps to attach to top and bottom plate	3D Print	
Float foam	Marine foam	Lab	
Stock			
Rack ground base	Multipurpose 6061 Aluminum 1/8" Thick X 2" Wide, 2 ft. Long	8975K582	$6.08
Float plates	Multipurpose 6061 Aluminum Sheet, 1/2" thick, 12" x 12"	8975K135	$62.03
Rack support bar	Anodized Multipurpose 6061 Aluminum Bar, 1/4" Thick x 1/4" Wide, 1 ft long	6023K35	$10.83
Top plate material	6061 1/8" thick aluminum, 12" by 36"	89015K241	$73.25
Bottom "plate"	Multipurpose 6061 Aluminum Sheet, 1/8" Thick, 12" x 12"	89015K18	$29.30
Fasteners			
Support shaft rods + housing	Stainless Steel Socket Head Screw, 1/4"-20 Thread Size, 3/4" Long, Packs of 10	92185A540	$3.99
Support shaft rods + housing	316 Stainless Steel Washer for 1/4" Screw Size, 0.281" ID, 0.625" OD, Packs of 100	90107A029	$8.06
Support shaft housing	18-8 Stainless Steel Nylon-Insert Locknut 1/4"-20 Thread Size, Packs of 50	91831A029	$6.27
Through float screws	18-8 Stainless Steel Socket Head Screw, 6-32 Thread Size, 3 1/2" Long, packs of 1	92196A955	$15.87
Through float screws	Stainless Steel Socket Head Screw 8-32 Thread size, 4" Long, Packs of 1	92196A213	$2.71
8-32 nuts	18-8 Stainless Steel Hex Nut 8-32 Thread Size, packs of 100	91841A009	$4.30
8-32 washers	18-8 Stainless Steel Washer for Number 8 Screw Size, 0.172" ID, 0.375" OD, packs of 100	92141A009	$2.07
6-32 nuts	18-8 Stainless Steel Hex Nut 6-32 Thread Size	91841A007	$4.33
6-32 washers	18-8 Stainless Steel Washer for Number 6 Screw Size, 0.156" ID, 0.312" OD	92141A008	$1.53
Rack ground brackets	18-8 Stainless Steel Socket Head Screw, 6-32 Thread Size, 7/8" Long, Pack of 100	92196A152	$9.25
Rack to support bar + casing	18-8 Stainless Steel Hex Drive Flat Head Screw, 82 Degree Countersink Angle, 6-32 Thread Size, 1/2" Long	92210A148	$6.29
Rack to ground and bar	18-8 Stainless Steel Nylon-Insert Locknut 6-32 Thread Size	91831A007	$6.20
Rack base brackets	304 Stainless Steel Corner Bracket, 1-3/16" x 1-3/16" x 1/2"	19155A34	$5.62
80-20 to top plate	T-Slotted Framing, End-Feed Nut and Button Head, for 1" and 25 mm High Rail, Packs of 4	47065T139	$3.05
Bottom plate to mooring	T-Slotted Framing, End-Feed Double Nut and Flanged Button Head, for 1" High Rail, Packs of 4	47065T147	$6.12

Accepted manuscript Not Copyedited

Downloaded from http://asmedigitalcollection.asme.org/mechanicaldesign/article-pdf/doi/10.1115/1.4070757/7582635/md-25-1640.pdf by guest on 05 January 2026

Journal of Mechanical Design. Received September 05, 2025;
Accepted manuscript posted January 5, 2026. doi:10.1115/1.4070757
Copyright © 2026 by ASME; reuse license CC-BY 4.0

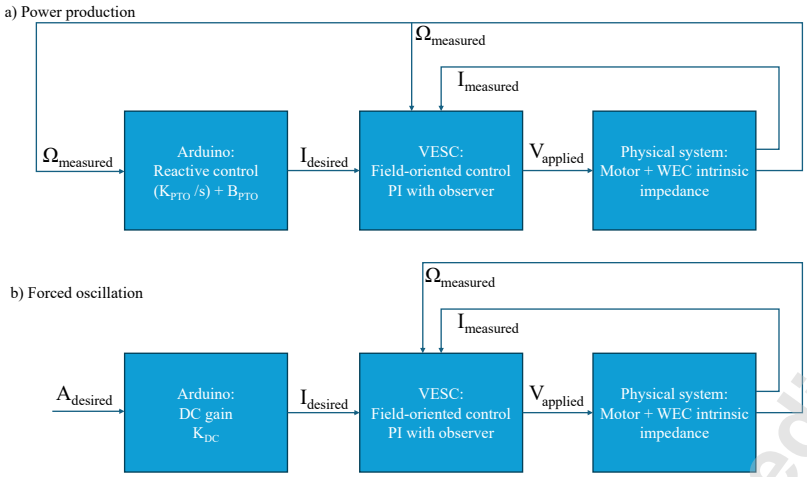

Fig. 16 Control diagram for forced oscillation and power production.

Table 9 Oscillating surge WEC bill of materials. All part numbers correspond with McMaster-Carr parts.

Component/System	Part Description	Part #	Unit Cost
PTO			
Pinion	M1.5, 36 Teeth, pressure angle 20° Stainless Steel		
Housing long bolts	18-8 Stainless Steel Hex Head Screw, 1/4"-20 Thread Size, 7" Long	92198A570	$3.27
Housing cylinder	Polycarbonate Rigid Round Tube, Clear, 4" ID x 4-1/4" OD x 12" L		$25.81
Bearings	Shielded ball bearing 8 mm shaft 16 mm housing OD	7804K117	$7.11
Motor attachment stock	Multipurpose 6061 Aluminum Rod, 1-3/4" Diameter, 1 ft	8974K68	$27.97
Motor shaft	Linear Motion Shaft, 420 Stainless Steel, 8 mm Diameter, 100 mm Long	6459K118	$8.93
Flap			
Weighting aluminum	Multipurpose 6061 Aluminum Sheets and Bars 1/2" thick 1.5" wide 6ft long	8975K42	$48.57
Flap foam	Marine foam	Lab	
Shaft bearings	Ultra-Corrosion-Resistant Mounted Acetal Ball Bearing for 5/8" Shaft Diameter	6357K42	$58.16
Flap shaft	D-Profile Rotary Shaft, 303 Stainless Steel, 5/8" Diameter, 36" Long	8632T159	$55.96
Flap acrylic	2-Pack Clear Acrylic Sheet Cast Plexiglass 12 x 18", 1/8" Thick		$25.98
Flap struts	Multipurpose 6061 Aluminum, 1/4" Thick x 12" Wide, 1 Foot Long	9246K13	$32.59
Strut to flap fasteners	18-8 Stainless Steel Socket Head Screw, 6-32 Thread Size, 2-1/2" Long, Packs of 25	92196A161	$7.63
Shaft collars	D-Profile Shaft Collar for 5/8" Diameter, 303 Stainless Steel	9687T448	$61.68
Fasteners			
Through float bolts	18-8 Stainless Steel Socket Head Screw 6-32 Thread Size, 2-1/2" Long Packs of 25	92196A161	$7.63
Framing brackets	Silver Gusset Bracket, 2" Long for 1" High Rail T-Slotted Framing	47065T736	$15.20
80-20 triangular	T-Slotted Framing, Silver Diagonal Brace for 1" High Single Rail, 6" Long	47065T186	$21.43
Motor housing attachment	T-Slotted Framing, Silver Surface Bracket, 2" Long for 2" High Double/Quad Rail	47065T257	$13.75

Accepted Manuscript Not Copyedited

Downloaded from http://asmedigitalcollection.asme.org/mechanicaldesign/article-pdf/doi/10.1115/1.4070757/7582635/md-25-1640.pdf by guest on 05 January 2026

Journal of Mechanical Design. Received September 05, 2025;
Accepted manuscript posted January 5, 2026. doi:10.1115/1.4070757
Copyright © 2026 by ASME; reuse license CC-BY 4.0

Table 10 Motor housing bill of materials. All part numbers correspond with McMaster-Carr parts.

Component/System	Part Description	Part #	Unit Cost
Motor housing spacers	Female Threaded Round Standoff, 18-8 Stainless Steel, 1/2" OD, 2" Long, 1/4"-20 Thread Size	91125A652	$4.47
Housing long bolts	18-8 Stainless Steel Hex Head Screw, 1/4"-20 Thread Size, 7" Long, Partially Threaded, packs of 1	92240A565	$2.92
Housing cylinder	Polycarbonate Rigid Round Tube, Clear, 4" ID x 4-1/4" OD x 12" L		$25.81
Bearings	Shielded ball bearing 8 mm shaft 16 mm housing OD	7804K117	$7.11
Motor attachment stock	Multipurpose 6061 Aluminum Rod, 1-3/4" Diameter, 1 ft	8974K68	$27.97
Motor bolts to spacer	18-8 Stainless Steel Socket Head Screw M4 x 0.7 mm Thread, 14 mm Long, packs of 100	91292A038	$11.45
Motor shaft	Linear Motion Shaft, 420 Stainless Steel, 8 mm Diameter, 100 mm Long	6459K118	$8.93
Brackets	Silver Corner Bracket, 1" Long for 1" High Rail T-Slotted Framing	47065T236	$7.92
Track roller for rack	Maintenance-Free Threaded Track Roller, Steel Flat Roller, 1" Diameter x 5/8" Wide Roller	6721K5	$33.65
Roller nuts	18-8 Stainless Steel Hex Nut 7/16"-20 Thread Size, ASTM F594, Packs of 10	92673A134	$2.85
Roller washers	316 Stainless Steel Washer for 7/16" Screw Size, 0.5" ID, 1.125" OD, Packs of 25	90107A032	$7.88
Motor to torque sensor mount	Headless Shoulder Screws 5.5 mm Shoulder Diameter, 10 mm Shoulder Length, packs of 5	94128A106	$6.29

Table 11 Electronics bill of materials

Component	Part Number + Link	Price/Unit	Voltage Range	Current Rating
Motor	CubeMars R80 KV110	$258.9	48 V	15 A (continuous) / 46 A (peak)
Motor Controller	Vesc 6 75V	$309.6	14 V - 63 V	80 A (continuous) / 120 A (max)
Oregon Power Supply	Chroma Model 62006P-100-25	$0	100V	25A
New PSU	MPS-6000S-60-1000	$1820	60V	100A
Brake Chopper / Brake Resistor	BC72-50 – Brake chopper	$156.3	12 V - 75 V	N/A
DC Busbar	Victron Energy Busbars 6 connectors	$25.25	70V	150A
Micro Reaction Torque Sensor		$175.99	-	-
Load Cell Transmitter	ATO Link	$81.27	-	-
Sensors and Logging	Vesc EXPRESS with CANBUS POWER Cable 2	$38.7	-	-
Fuse	120A fuse for Vesc / ESC	$12	100V	180A
Diode	1N5408	$0.19	1000V	3A
Busbar Connectors	10pcs 6 Awg - 5/16" (M8) Battery Copper Lugs	$8.39	-	-
Crimping Tool	TEMCo Hammer Lug Crimper Tool	$16.95	-	-
Motor Wire Connectors	Amass MR30 18AWG LiPo Pigtail w/ Protective Sleeve	$15.99	-	-
Protective Wire Wrapping	100ft - 1/2 inch PET Expandable Braided Sleeving	$15.99	-	-
Long UWV/XYZ Wires for Motor	BNTECHGO 10 Gauge Silicone Wire Spool	$165	-	-
Bullet Connectors	Apex RC Products 5.5mm Gold Plated Bullet Connectors	$12.99	-	-
microSD Card	SC0251L	$7.94	-	-
Waterproof Connectors	NAOEVO 5 Pin Connector Waterproof	$18.99	-	-
Waterproof Heatshrink	Kuject Heat Shrink Solder Seal Wire	$7.99	-	-
Buck Converter	Buck Converter 240W Input (30V-120V)	$20	-	-
Arduino Cables (4 ct)	Digikey	$7.99	-	-
Hall Sensor Cable	SM05B-GHS-TB (uncertain)	-	-	-
Crimped Wires, AWG 28	ASZHSZH28K51	-	-	-
Backup Resistor Bank	TE2500B1R0J	$189	-	-

Accepted Manuscript Not Copyedited

Downloaded from http://asmedigitalcollection.asme.org/mechanicaldesign/article-pdf/doi/10.1115/1.4070757/7582635/md-25-1640.pdf by guest on 05 January 2026

Journal of Mechanical Design. Received September 05, 2025;
Accepted manuscript posted January 5, 2026. doi:10.1115/1.4070757
Copyright © 2026 by ASME; reuse license CC-BY 4.0

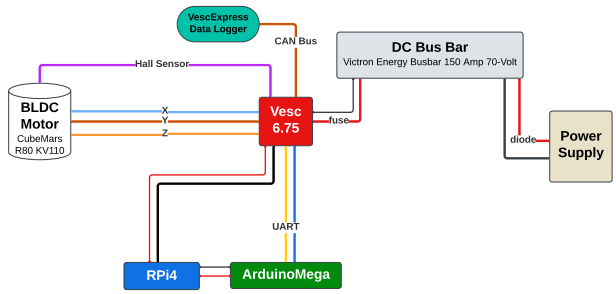

Fig. 17 Electrical system used during array experiments.

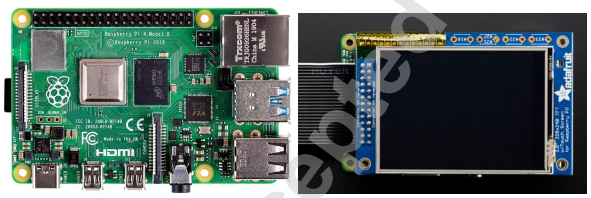

Fig. 18 RPi 4 Model B (left) and RPi with TFT screen (right).

Accepted Manuscript Not Copyedited

Downloaded from http://asmedigitalcollection.asme.org/mechanicaldesign/article-pdf/doi/10.1115/1.4070757/7582635/md-25-1640.pdf by guest on 05 January 2026

Journal of Mechanical Design. Received September 05, 2025;
Accepted manuscript posted January 5, 2026. doi:10.1115/1.4070757
Copyright © 2026 by ASME; reuse license CC-BY 4.0

List of Figures

List of Tables

Accepted Manuscript Not Copyedited

Downloaded from http://asmedigitalcollection.asme.org/mechanicaldesign/article-pdf/doi/10.1115/1.4070757/7582635/md-25-1640.pdf by guest on 05 January 2026